Cell Reports

Article

G6PD deficiency triggers dopamine loss and the initiation of Parkinson's disease pathogenesis

Graphical abstract

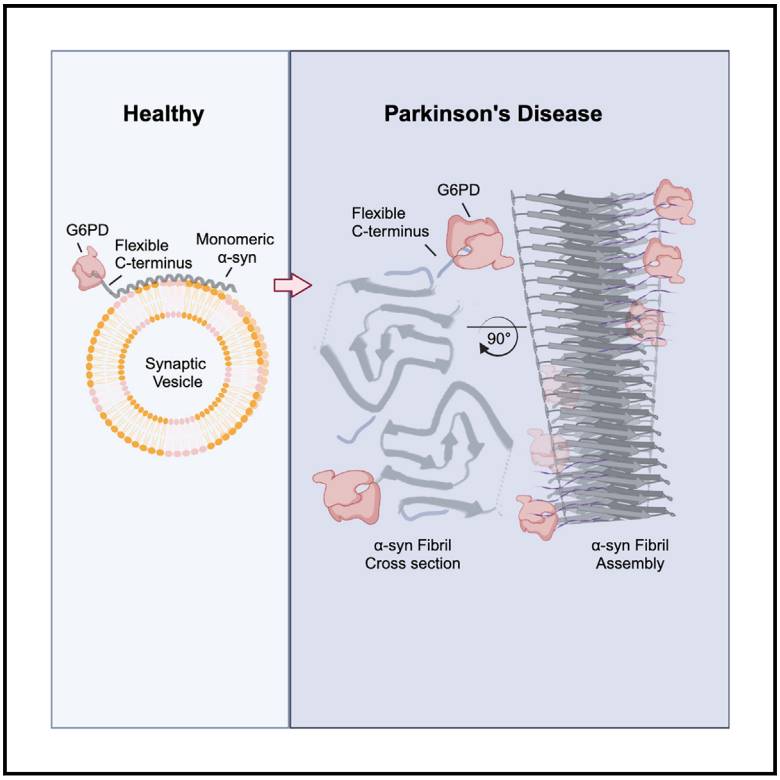

Highlights

- α-syn binds to and anchors G6PD to synaptic vesicles
- α-syn fibrilization inhibits G6PD function and impairs redox homeostasis
- Loss of G6PD function phenocopies Parkinson's disease
- Restoration of G6PD activity rescues dopamine signaling in Parkinson's disease

Authors

Morgan G. Stykel, Shehani V. Siripala, Eric Soubeyrand, ..., Tariq A. Akhtar, Joel C. Watts, Scott D. Ryan

Correspondence

scott.ryan@ucalgary.ca

In brief

Stykel et al. show that G6PD missense mutations increase the risk of PD diagnosis and that α-syn accumulation leads to G6PD dysfunction and deposition into Lewy bodies. This leads to loss of redox homeostasis and dopamine oxidation that can be rescued pharmacologically by either N-acetylcysteine (NAC) or the G6PD agonist AG-1.

Stykel et al., 2025, Cell Reports *44*, 115178
January 28, 2025
https://doi.org/10.1016/j.celrep.2024.115178

CellPress

Cell Reports

CellPress
OPEN ACCESS

Article

G6PD deficiency triggers dopamine loss and the initiation of Parkinson's disease pathogenesis

Morgan G. Stykel,[1] Shehani V. Siripala,[1,2,8] Eric Soubeyrand,[1,8] Carla L. Coackley,[1] Ping Lu,[2] Suelen Camargo,[2] Sharanya Thevasenan,[2] Gerardo Balderas Figueroa,[2] Raphaella W.L. So,[3,4] Erica Stuart,[3,4] Rachi Panchal,[5] Elissavet-Kalliopi Akrioti,[6] Jeffery T. Joseph,[7] Omid Haji-Ghassemi,[5] Era Taoufik,[6] Tariq A. Akhtar,[1] Joel C. Watts,[3,4] and Scott D. Ryan[1,2,9,*]

[1]Department of Molecular and Cellular Biology, The University of Guelph, Guelph ON, Canada
[2]Department of Clinical Neuroscience, University of Calgary, Calgary, AB, Canada
[3]Tanz Centre for Research in Neurodegenerative Diseases, University of Toronto, Toronto, ON, Canada
[4]Department of Biochemistry, University of Toronto, Toronto, ON, Canada
[5]Department of Biological Sciences, University of Calgary, Calgary, AB, Canada
[6]Laboratory of Cellular and Molecular Neurobiology-Stem Cells, Hellenic Pasteur Institute, Athens, Greece
[7]Department of Pathology and Laboratory Medicine, University of Calgary, Calgary, AB, Canada
[8]These authors contributed equally
[9]Lead contact
*Correspondence: scott.ryan@ucalgary.ca
https://doi.org/10.1016/j.celrep.2024.115178

SUMMARY

Loss of dopaminergic neurons in Parkinson's disease (PD) is preceded by loss of synaptic dopamine (DA) and accumulation of proteinaceous aggregates. Linking these deficits is critical to restoring DA signaling in PD. Using murine and human pluripotent stem cell (hPSC) models of PD coupled with human postmortem tissue, we show that accumulation of α-syn micro-aggregates impairs metabolic flux through the pentose phosphate pathway (PPP). This leads to decreased nicotinamide adenine dinucleotide phosphate (NADP/H) and glutathione (GSH) levels, resulting in DA oxidation and decreased total DA levels. We find that α-syn anchors the PPP enzyme G6PD to synaptic vesicles via the α-syn C terminus and that this interaction is lost in PD. Furthermore, G6PD clinical mutations are associated with PD diagnosis, and G6PD deletion phenocopies PD pathology. Finally, we show that restoring NADPH or GSH levels through genetic and pharmacological intervention blocks DA oxidation and rescues steady-state DA levels, identifying G6PD as a pharmacological target against PD.

INTRODUCTION

The decline of voluntary motor function in Parkinson's disease (PD) is caused, in part, by loss of A9 dopaminergic neurons in the substantia nigra pars compacta. Pathophysiological damage and loss of function of these neurons precede neurodegeneration and contribute to the early phases of the movement impairments through loss of synaptic neurotransmission.[1–3] Early pathologies include loss of caudal dopamine[2,3] and accumulation of oligomeric species of α-syn that have been implicated in both sporadic and familial cases of PD. The A53T α-syn protein variant (G209A mutation in the *SNCA* gene), which is associated with early disease onset,[4] has highlighted the role of α-syn aggregation in the loss of dopamine (DA) and other neuronal cell types in multiple PD model systems. Transgenic overexpression of A53T mutant α-syn in mice leads to neuronal dysfunction and behavioral impairments that parallel the formation of α-syn immune-reactive deposits in neurites of both cortical and midbrain neurons.[5,6] Ectopic exposure to α-syn pre-formed fibrils (PFFs) permits the modeling of fibrillogenesis, similarly inducing widespread axonal neuropathology, decreased synaptic function, and subsequent neuronal death.[7–9] While *SNCA* mutations are causal in rare familial forms of PD and dramatically increase the risk of both motor and non-motor disease symptoms (including dementia),[4,10] the prevalence of α-syn aggregates in Lewy neurites found in the brains of patients with idiopathic disease emphasizes the need to understand how α-syn accumulation leads to early synaptic dysfunction in nigrostriatal neurons.

Many speculate that the pacemaking activity (fast-spiking Ca^{2+} transients) of dopaminergic neurons makes them uniquely susceptible to reactive oxygen and nitrogen species (RONS) production.[11,12] RONS, such as superoxide anions, nitric oxide, and dopamine-ortho-quinone (Ox-DA) are among the free radicals that accumulate in PD neurons and are closely tied to impaired neuronal function.[13–15] These free radicals can modify proteins through redox-based reactions with cysteine thiols

that include sulfenylation, S-nitrosylation, and DA-protein adduct formation. Evidence suggests that redox-based modifications are critical effectors of protein misfolding and subsequent aggregation.[16–22] Two major scavenging pathways reduce oxidized cysteine in cells: the thioredoxin reductase (Trx) family of redox sensors that includes glutaredoxin (Grx) and the indirect glutathione reductase system (for a review, see Stykel and Ryan[17]). Trx removes the sulfide group from the protein-S-R group through either Trx-mediated transfer or Trx–disulfide bond formation that reduces the oxidized cysteine. Alternatively, the glutathione reductase system utilizes glutathione (GSH), which reacts directly with the sulfide group of oxidized cysteines, transferring the oxidized group to the thiol of the cysteinyl group on GSH, generating glutathione disulfide (GSSG). This can be cycled back to GSH through the activity of GSH reductase (GR) and the co-factor NADPH. Thus, the ability to generate NADPH is critically tied to the redox homeostasis of DA neurons. How these systems are influenced by α-syn protein or the α-syn micro-aggregates that accumulate in disease is poorly understood.

The generation of human isogenic induced pluripotent stem cell (hiPSC) and human embryonic stem cell (hESC) models of familial PD has facilitated the analysis of PD pathology at the cellular level,[23] allowing us to contrast A9-type DA neurons (hNs) harboring mutations with isogenic, mutation-corrected controls.[24] These neurons show early synaptic deficits, altered network connectivity, and accumulation of α-syn into heat-stable, detergent-resistant deposits.[25,26] Using these systems, we describe a novel mechanism in which α-syn binds to and anchors the pentose phosphate pathway (PPP) enzyme G6PD to synaptic vesicles, facilitating the localized synthesis of NADPH that functions to maintain GSH-mediated redox homeostasis. In PD neurons, accumulation of misfolded α-syn oligomers and immature protofibrils (henceforth referred to as α-syn microaggregates) results in loss of G6PD from synaptic vesicles and impairs PPP-mediated synthesis of NADPH and GSH, resulting in increased Ox-DA formation and decreased overall DA levels. We further determined that G6PD missense mutations that lead to G6PD metabolic dysfunction have a significant association with initial PD diagnosis and that G6PD silencing phenocopies pathological α-syn accumulation and DA oxidation hiPSC-derived neurons. Finally, we show that restoring the NADPH/TRX system through overexpression of TRX or normalizing free NADPH and GSH levels through pharmacological administration of either N-acetylcysteine (NAC) or the G6PD agonist AG-1 blocks DA oxidation and rescues steady-state DA levels.

RESULTS

Neurons from *SNCA*-mutant hPSCs demonstrate synucleinopathy coupled with oxidized dopamine

To understand how α-syn micro-aggregates relate to early decreases in DA levels in neurons, we compared hiPSC-derived clones harboring the G209A-*SNCA* mutation (A53T protein variant) to isogenic genome-corrected controls (Corr).[23,24] We also analyzed hESC-derived clones that allow for comparison of wild-type (WT) α-syn against A53T α-syn, wherein the mutation was introduced. In both sets of isogenic lines, floor-plate induction of dopaminergic neurons reliably produced equivalent numbers of tyrosine hydroxylase (TH)-positive neurons (Figures 1A and 1B). Post-translational phosphorylation of α-syn at serine 129 (PS129) enhances its tendency to misfold and form microaggregates associated with PD pathogenesis.[27,28] PS129-positive cell numbers were significantly increased in A53T-hNs relative to isogenic controls (Figures 1A and 1B). Moreover, western blot analysis of PS129 showed increased PS129 deposition in *SNCA*-mutant lines from both hESC (Figures 1C and 1D) and hiPSC (Figures 1H and 1I) origin, yielding an increased ratio of phospho-α-syn relative to total α-syn (Figures 1D–1I). These data show that α-syn is aberrantly phosphorylated in differentiated A53T-hNs relative to isogenic control-hNs, consistent with the form of α-syn associated with pathologic aggregates in the PD brain.[27,28]

To determine whether the accumulation of α-syn microaggregates impacted levels of DA in A53T-hNs, we measured total DA levels. High-performance liquid chromatography (HPLC) analysis of total DA levels from hESC WT and A53T hNs (Figure 1E) or hiPSC-A53T and corrected hNs (Figure 1J) show reduced total DA levels in PD neurons relative to isogenic controls. Since DA loss in PD can be explained, in part, by increased oxidation of DA and formation of DA protein adducts, we measured the accumulation of DA protein adducts in both hESC-derived (Figures 1F and 1G) and hiPSC-derived (Figures 1K–1L) systems. A significant increase in Ox-DA protein adduct formation was observed in α-syn mutant neurons relative to controls (Figures 1F, 1G, 1K, and 1L), coincident with the decrease in levels of total DA. Moreover, increasing redox stress via exposure to the mitochondrial toxin rotenone (Figures 1K and 1L) dramatically increased Ox-DA protein adduct formation in A53T-hNs relative to both Corr hNs and vehicle treated ones, suggesting that α-syn mutation significantly lowers the threshold for DA oxidation in response to oxidative stress. Collectively, these data show that the accumulation of α-syn microaggregates is associated with loss of DA in PD neurons and that this loss can be attributed to increased Ox-DA protein adduct formation.

α-syn mutant neurons show a decrease in flux through the PPP

To gain insight into why mutation in α-syn or accumulation of α-syn microaggregates increases the propensity of DA oxidation, we conducted an unbiased metabolic study to determine whether metabolic alterations could explain the loss of redox homeostasis. Metabolite profiling of hiPSC-derived corrected and A53T-hNs was performed following labeling of neurons with U-C^{13}-glucose. Isotopically labeled metabolites were then identified by reversed-phase ion-pair (RPIP) mass spectrometry in negative mode. The top metabolites altered by fold change in A53T-hNs relative to corrected ones are depicted as a heatmap (Figure 2A), whereas the top metabolites altered *p*-value are depicted by volcano plot (Figure 2B). Pathway-specific analysis (Figures 2C–2E) suggested that flux through glycolysis was altered, as was the production of redox substrates, while adenosine phosphate metabolism was not significantly changed. While the observed decrease in fructose-1,6-bisphosphate (F-1,6-P) and dihydroxyacetone phosphate

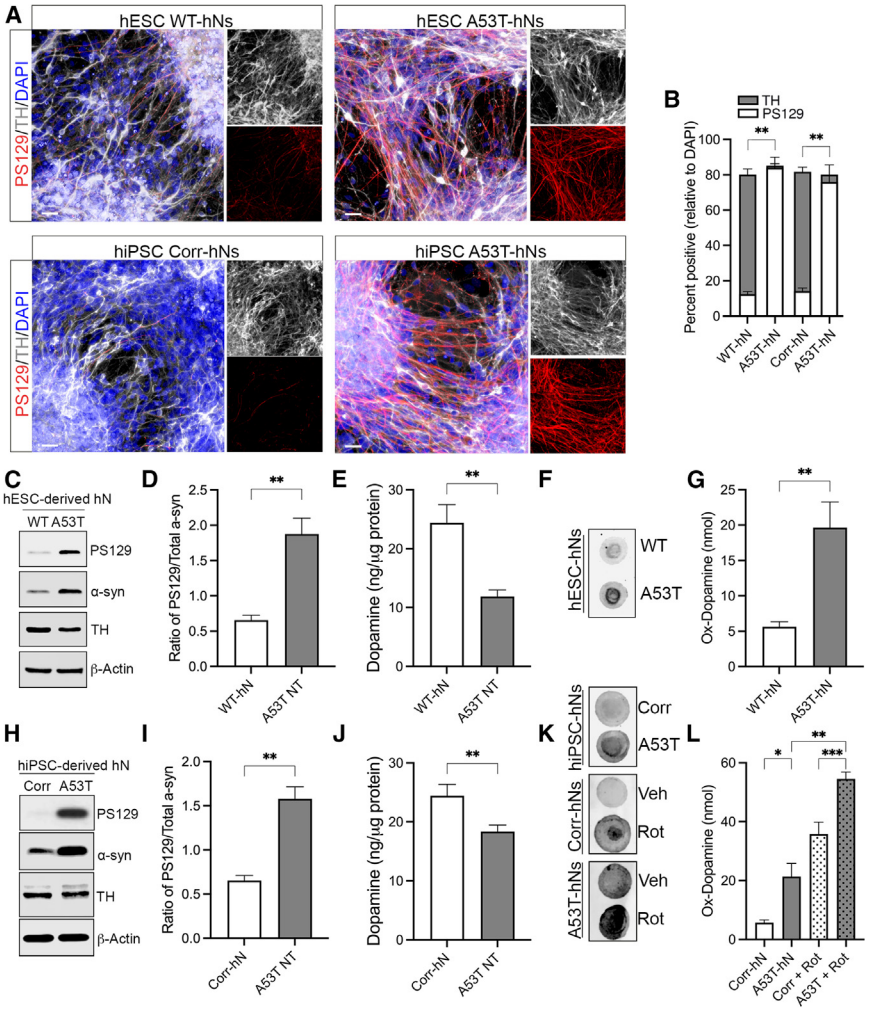

Figure 1. α-syn mutant hNs show decreased levels of DA and increased levels of Ox-DA

(A) Accumulation of α-syn PS129 protein in TH-positive DA neurons derived from hESC-WT and A53T hNs or hiPSC-A53T and corrected hNs. Scale bar: 50 μm.

(B) Quantification of α-syn PS129 and TH-positive cells relative to DAPI. Data represent mean ± SEM. $^{**}p < 0.01$ by t test. $n = 6$ independent coverslips over three differentiations. Days *in vitro* (DIV): 55–65. Scale bar: 50 μm.

(C, D, H, and I) Ratiometric increase of α-syn PS129 protein relative to total α-syn in hESC-derived WT and A53T hNs (C and D) or hiPSC-derived A53T and corrected hNs (H and I). Data represent mean ± SEM. $^{**}p < 0.01$ by t test. $n = 6$ independent samples over three differentiations. DIV: 55–65.

(E–G and J–L) HPLC analysis of total DA levels coupled to nIRF analysis of Ox-DA levels from hESC-WT and A53T hNs (E–G) or hiPSC-A53T and corrected hNs (J–L) shows reduced total DA levels coincident with increased Ox-DA levels in PD neurons. Data represent mean ± SEM. $^{**}p < 0.01$ by t test. $n = 6$ independent samples over three differentiations. DIV: 55–65.

(K and L) Rotenone exposure further increases Ox-DA accumulation. $^{**}p < 0.01$ by ANOVA followed by Tukey's post hoc test. $n = 6$ independent samples over three differentiations.

metabolite levels can result either from impaired glycolytic metabolism of G6P to fructose 6-phosphate (F-6-P) (and subsequently to F-1,6-P) or through impaired PPP-mediated generation of F-6-P, the decrease in GSH production coupled with the lack of change in ATP production strongly implicated the PPP in this metabolic deficit. We therefore performed a targeted metabolic analysis of PPP flux relative glycolytic flux using [1,2]-C^{13}-glucose (Figure 2F). While the fold change in M+1 labeled lactose (PPP flux) and M+2 labeled lactose (Glycolytic flux) suggested that both pathways were impaired in A53T-hNs relative to corrected, a ratiometric comparison of the fold changes in M+1/M+2 lactate fraction showed a decrease in A53T-hNs (Figure S1). Given that neurons rely more heavily on the PPP for redox homeostasis through $NADPH/H^+$ and GSH cycling (Figure 2G), we sought to further explore PPP impairment. We reasoned that if α-syn association with PPP enzymes is functionally relevant, then we should see a decrease in both $NADPH/H^+$ and GSH levels in A53T-hNs relative to WT-hN. We therefore, measured the ratiometric levels of $NADPH/H^+$ to $NADP^+$ in both hESC-derived and hiPSC-derived A53T-hNs and controls (Figures 2H and 2I) and observed a significant decrease in the ratio of $NADPH/H^+$ to $NADP^+$ in PD mutant neurons relative to isogeneic controls (Figures 2G and 2H). $NADP^+$ conversion to $NADPH/H^+$ through the PPP is facilitated by the enzyme G6PD. We therefore, directly assayed G6PD activity in hiPSC-derived A53T-hNs and corrected hNs (Figure 2J) and found G6PD activity to be significantly reduced in PD neurons. Finally, measurement of the ratiometric levels of GSH to GSSG in both hESC-derived and hiPSC-derived A53T-hNs and controls (Figures 2K–2L) confirmed a decrease in GSH/GSSG in PD neurons relative to isogenic controls. Collectively, these data suggest a decrease in flux through the PPP that leads to a decrease in GSH cycling and loss of redox homeostasis.

PPP enzymes are tethered to synaptic vesicles and this tethering is reduced in PD model systems

We next sought to investigate the relationship between the decreased flux through the PPP in A53T-hNs and the increase in Ox-DA adduct formation observed in these neurons. We postulated that if PPP flux alters Ox-DA adduct formation in synucleinopathy models, then perhaps PPP enzymes are bound to either α-syn or synaptic vesicles. To evaluate this postulate, we performed cellular fractionation on hiPSC-derived A53T and corrected hNs in order to enrich for synaptic vesicles. After the separation of nuclei and mitochondria, vesicle-enriched cellular fractions were subjected to a sucrose gradient to isolate density-enriched fractions containing synaptic vesicles

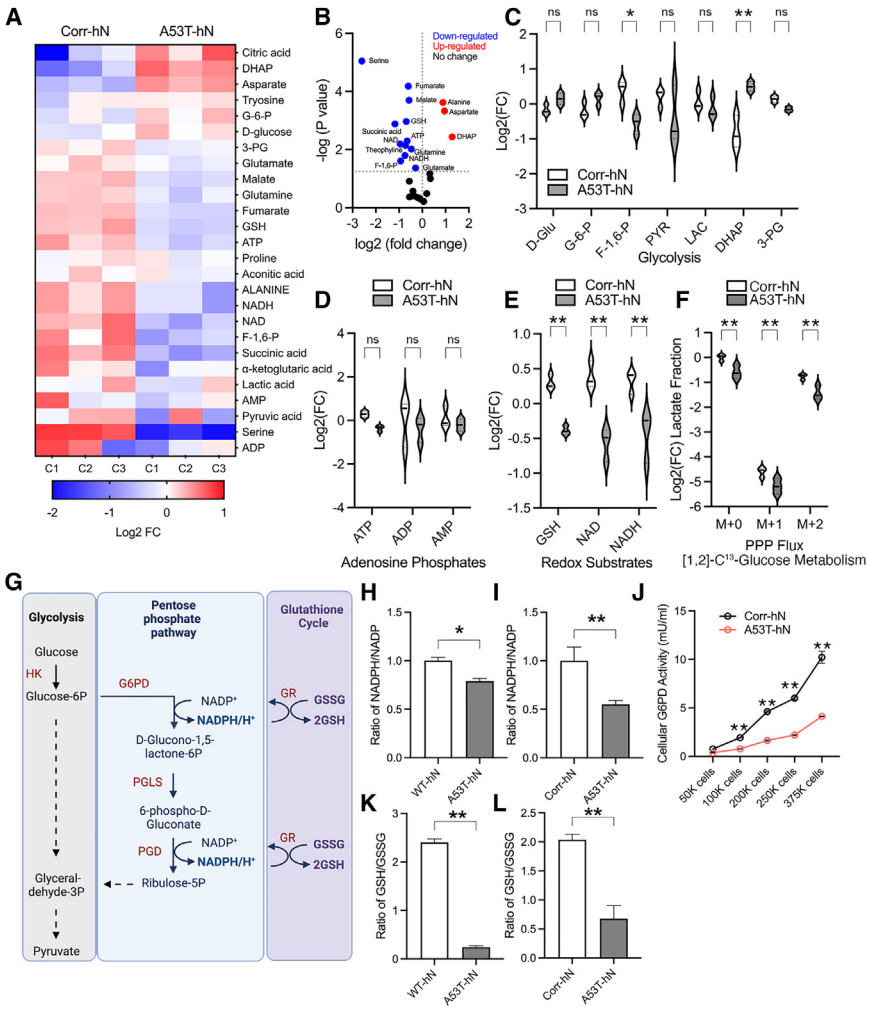

Figure 2. α-syn mutant hNs show flux through the PPP

(A–E) Profiling of U-C^{13}-glucose metabolism in hiPSC-derived hNs shows the major metabolites altered in A53T relative to corrected (A and B) grouped by metabolite class; glycolytic (C), adenosine phosphates (D) and redox substrates (E). $^{*}p < 0.05$, $^{**}p < 0.01$ by t test. Data represent mean ± SEM. $n = 3$ independent samples.

(F) Profiling of [1,2]-C^{13}-glucose metabolism to lactate shows that both glycolytic (M+2) and PPP (M+1) flux is decreased in A53T-hNs relative to Corr-hNs. $^{**}p < 0.01$ by t test. Data represent mean ± SEM. $n = 3$ independent samples.

(G) Schematic of the PPP, which regulates redox homeostasis via the GSH cycle.

(H and I) Ratiometric levels of NADPH/NADP were assessed in hESC-derived WT and A53T hNs (H) or hiPSC-A53T and corrected hNs (I) to confirm a decrease in flux through the PPP. $^{**}p < 0.01$ by t test. Data represent mean ± SEM. $n = 6$ independent samples over three differentiations. DIV: 55–65.

(J) Measurement of G6PD activity in hiPSC-A53T and corrected hNs shows significantly reduced G6PD activity in hiPSC-A53T-hNs relative to control. Data represent mean ± SEM. $n = 6$. $^{**}p < 0.01$ by ANOVA followed by post hoc Tukey test.

(K and L) Ratiometric levels of GSH/GSSG were assessed in hESC-derived WT and A53T hNs (K) and hiPSC-A53T and corrected hNs (L) to confirm a decrease in GSH cycling. $^{**}p < 0.01$ by t test. Data represent mean ± SEM. $n = 8$ independent samples over three differentiations. DIV: 55–65.

(Figures 3A and 3B and S2A). Synaptic vesicle-enriched fractions were then probed by western blot for PPP enzymes, with a focus on those involved in $NADPH^{+}$ synthesis, as well as for total α-syn (Figure 3A). We found that synaptic vesicle enriched fractions from A53T-hNs contained the PPP enzymes; G6PD, 6-phosphogluconolactonase (PGLS), and 6-phosphogluconate dehydrogenase (PGD) (Figure 3A). Moreover, we found there was a reduction in levels of G6PD and α-syn on A53T synaptic vesicles relative to control (Figures 3A and 3B). These data suggested that PPP enzymes may be onboarded onto synaptic vesicles, and that localization of G6PD specifically to synaptic vesicles is attuned to α-syn mutation or microaggregate formation. We therefore performed super-resolution microscopy to visualize G6PD relative to both the synaptic vesicle marker synaptophysin and either α-syn-PS129 (Figures 3C–3F) or total α-syn (Figures S2B–S2E). A distance analysis (DiAna)[29] that measures the distance between each punctum was subsequently performed to assess the proximity of G6PD to synaptophysin (Figure 3D) or G6PD to α-syn-PS129 (Figure 3G). DiAna showed that G6PD and α-syn-PS129 or total α-syn are closer to each other and farther from synaptic vesicles in A53T-hNs relative to WT hNs (Figures 3D–3F and S2C–S2E). We reasoned that, if hPSC-derived neurons show evidence of early aggregate deposition, and these aggregates contain G6PD, then, in late-stage disease, G6PD should be present in Lewy bodies (LBs). Therefore, we performed immunohistochemistry for α-syn and G6PD on postmortem brain sections from three people with PD displaying striatal LB deposition (LBD) and three clinically normal case controls (Figures 3G, 3H, and S2F). In controls, G6PD was diffusely expressed throughout cells, and α-syn staining was negative for LB deposits. In PD/LBD cases, however, G6PD staining was consistent with that of an LB deposit. Collectively, these data suggest that G6PD is present at the synaptic vesicles in healthy neurons; however, when α-syn is mutated or misfolded, G6PD is released from the vesicle and drawn into LB aggregates.

To gain insight into whether the observed effect of α-syn on PPP flux and localization of PPP enzymes to synaptic vesicles was a consequence of α-syn mutation specifically or, more broadly, a result of α-syn misfolding and aggregation, we moved to an *in vivo* model system that facilitates the study of α-syn fibrilization. Injection of α-syn PFFs into the striatum of WT mice

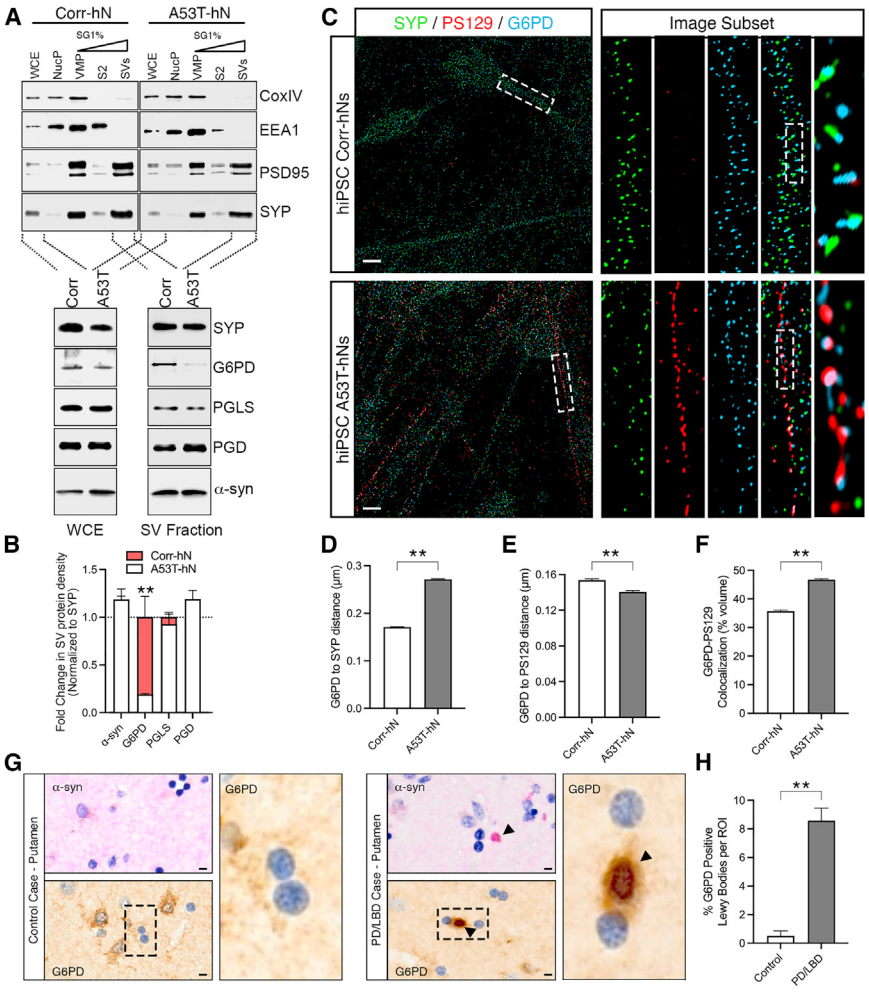

Figure 3. Synaptic tethering of the PPP enzyme G6PD is reduced in α-syn mutant hNs

(A and B) Sucrose gradient (SG)-enriched synaptic vesicle (SV) fractions from hiPSC-derived A53T and corrected hNs were probed for PPP enzymes and α-syn, and the amount of SV-associated protein relative to input was quantified (B). WCE, whole-cell extract; NucP, nuclear pellet; VMP, vesicle and mitochondrial pellet; S2, supernatant 2. $^{*}p < 0.05$, $^{**}p < 0.01$ by ANOVA followed by Tukey's post hoc test. Data represent mean ± SEM. $n = 3$ independent differentiations. DIV: 55–65.

(C) Super-resolution micrographs of hiPSC-derived corrected and A53T hNs immunolabeled for G6PD and α-syn-PS129 relative to synaptophysin (SYP). Scale bar: 50 μm.

(D and E) Distance analysis (DiAna) of G6PD relative to SYP (D) and α-syn-PS129 (E), coupled with colocalization analysis (F), shows that, in A53T-hNs, G6PD moves away from SVs while moving closer to α-syn-PS129. $^{**}p < 0.01$ by t test. Data represent mean ± SEM. 4 independent coverslips over three differentiations were used to generate data. n = 10,000–12,000 individual distance measurements. DIV: 55–65.

(G and H) Immunohistochemistry of G6PD and α-syn in the putamen of human control or PD/LBD cases shows an increase in LB-like structures that are positive for G6PD. $^{**}p < 0.01$ by t test. Data represent mean ± SEM. $n = 6$ control and 6 LBD cases. Scale bar: 10 μm.

causes an aggregation of endogenously expressed α-syn that spreads through anatomically connected regions of the brain, distal to the inoculation site.[8,30,31] When PFFs are propagated in hemizygous TgM83 synucleinopathy mice, which express A53T α-syn under the prion protein promoter, animals develop locomotor deficits beginning around 120 days post inoculation coupled to synucleinopathy.[32] TgM83 hemizygous animals were inoculated with either α-syn monomers or PFFs and then euthanized at either 90 or 120 day, representing pre-phenotypic and phenotypic onset time points, respectively.[32] Within this transition period, animals show a significant shift in the ratio of PS129 to total α-syn, with PFF-inoculated animals showing significantly increased PS129 levels by 120 days post inoculation (Figures 4A and 4B). Moreover, a shift in G6PD and α-syn protein deposition into detergent-insoluble fractions was also evident by principal-component analysis of lysates (Figures S3A–S3C). Despite the accumulation of pathological α-syn, no increase in cell death in striatal neurons was observed (Figures S3D and S3E). We next assessed PPP flux by measuring the ratiometric levels of $NADPH^{+}/H^{+}$ to $NADP^{+}$ from 90 to 120 days post inoculation and observed a significant decrease in this ratio in PFF-inoculated animals relative to controls (Figure 4C). HPLC analysis of total DA levels in mouse striatum 90 (Figure 4D) and 120 days post inoculation (Figure 4E) similarly showed a loss of striatal DA specifically in PFF-inoculated animals at 120 days post exposure (Figure 4E), which corresponded with a significant increase in Ox-DA protein adduct formation in PFF-exposed animals relative to monomer-exposed animals (Figure 4F). To confirm that these events were related to a loss of G6PD from synaptic vesicles, we developed a stepwise fractionation approach that enabled us first to purify synaptosomes and then purify synaptic vesicles from synaptosomal preparations rather than simple enrichment (Figures 4G and S3F). Purified synaptic vesicle fractions from mouse striatum were positive for the PPP enzymes G6PD, PGLS, and PGD (Figure 4H). Moreover, synaptic vesicles derived from animals 120 days post PFF inoculation showed a marked reduction in the proportion of G6PD present relative to synaptic vesicles isolated from monomer-exposed animals (Figures 4H and S3G). This was consistent with super-resolution microscopy of G6PD and PS129-α-syn in striatal sections from PFF- and monomer-inoculated animals (Figures 4I–4K). DiAna showed that G6PD and α-syn-PS129 are closer to each other in PFF-inoculated animals than in monomer-inoculated controls (Figures 4I–4K). To confirm that α-syn microaggregate formation altered the tethering of PPP enzymes to synaptic vesicles, we exposed WT primary neurons to PFFs for 7 days and again purified synaptic

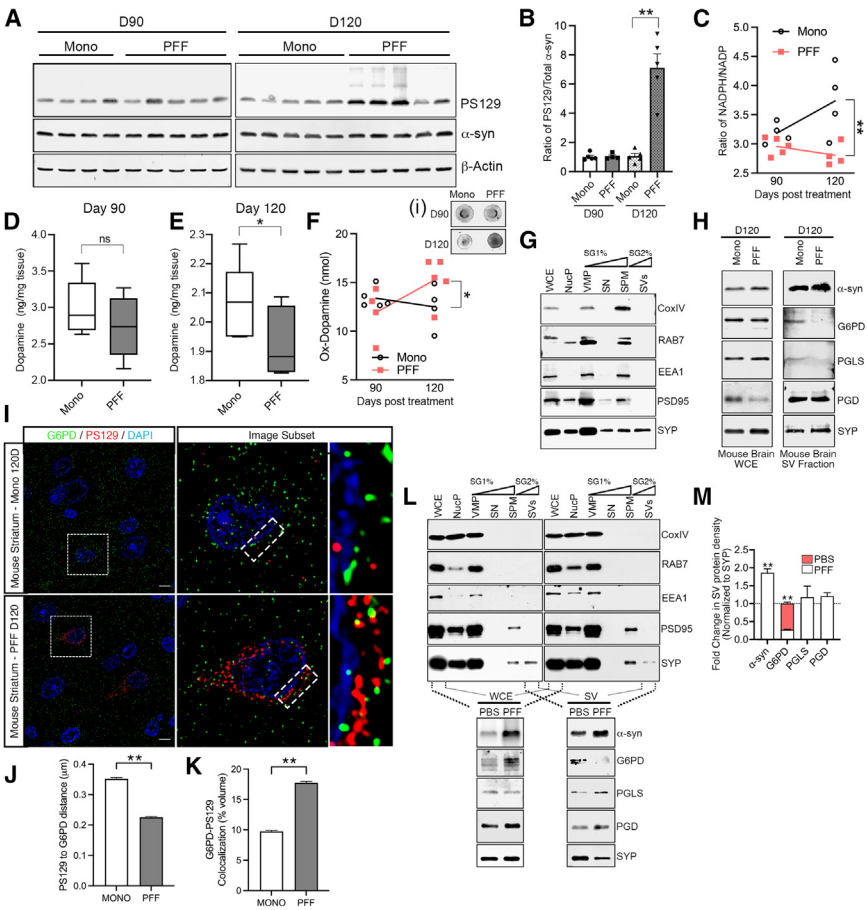

Figure 4. PFF-inoculated animals show decreased total DA and increased Ox-DA coupled to loss of G6PD from SVs

(A and B) TgM83 heterozygous animals were inoculated with either α-syn monomers (mono) or pre-formed fibrils (PFFs) and sacrificed either 90 or 120 day post inoculation. Lysates were probed for total α-syn and α-syn-PS129 (A), and the ratio of PS129/total α-syn was quantified (B). $^{**}p < 0.01$ by multivariate analysis of variance (MANOVA) followed by Tukey's post hoc test. Data represent mean ± SEM. n = 4–5 animals per condition.

(C) Ratiometric levels of NADPH/NADP were assessed to confirm a decrease in flux through the PPP. $^{**}p < 0.01$ by MANOVA followed by Tukey's post hoc test. Data represent mean ± SEM. n = 4–5 animals per condition.

(D and E) HPLC analysis of total DA levels 90 (D) and 120 (E) days post inoculation. $^{*}p < 0.05$ by t test. Data represent mean ± minimum and maximum. n = 4–5 animals per condition. n.s., not significant.

(F) nIRF quantification of Ox-DA blots (inset). $^{**}p < 0.01$ by MANOVA followed by Tukey's post hoc test. Data represent mean ± SEM. n = 4–5 animals per condition.

(G and H) Tandem SGs were employed to purify SVs from mouse brain (H). Pooled SV s from either mono or PFF-inoculated animals 120 days post inoculation were probed for PPP enzymes and α-syn. SN, supernatant; SPM, synaptosome.

(I–K) Super-resolution micrographs of hemizygous TgM83 animals inoculated with either α-syn monomers (mono) or PFFs and sacrificed ~120-day post inoculation were immunolabeled for G6PD and α-syn-PS129. DiAna of G6PD and relative to α-syn-PS129 (J), coupled with colocalization analysis (K), shows that G6PD moves closer to α-syn-PS129 in PFF-inoculated animals. $^{**}p < 0.01$ by t test. Data represent mean ± SEM. 6 mono and 7 PFF inoculated animals were used to generate data. n = 10,000–12,000 individual distance measurements. Scale bar: 10 μm.

(L and M) SG-enriched SV fractions from primary neurons exposed to PFF- or vehicle (PBS)-inoculated animals (L) were probed for PPP enzymes and α-syn, and the proportion of SV-associated protein relative to input was quantified (M). $^{**}p < 0.01$ by ANOVA followed by Tukey's post hoc test. Data represent mean ± SEM. n = 3 independent cultures.

vesicles (Figures 4L, 4M, and S3H). We found the PPP enzymes G6PD, PGLS, and PGD in purified synaptic vesicle fractions (Figures 4L and 4M). Moreover, there was again a proportional reduction in G6PD levels on synaptic vesicles isolated from PFF-exposed neurons relative to vehicle-exposed neurons (Figures 4L–4M and S3I). Collectively, these data argue (1) that PPP enzymes are tethered to synaptic vesicles, (2) that the observed deficit in PPP flux in PD model systems is a result of α-syn loss of function due to misfolding and pathological accumulation, and (3) that α-syn fibrilization results in loss of G6PD location to the synaptic vesicle.

Decreased G6PD enzyme activity is linked to PD onset through altered α-syn binding

To understand how α-syn might facilitate G6PD tethering to synaptic vesicles, we employed AlphaFold 3 (collabfold) to perform AI-guided predictions of the structural nature of the G6PD-α-syn interaction with both monomers and fibrils (Figures 5A–5F). AlphaFold3 prediction of the G6PD-α-syn interaction shows α-syn in an α-helical conformation rather than as an intrinsically disordered random coil when G6PD bound, consistent with the α-syn structural conformation associated with lipid vesicles (Figures 5A and 5B). Moreover, α-syn is predicted to bind G6PD via its C terminus (Figures 5A–5C), which remains flexible when in an α-helical conformation,[33] again consistent with a functional role in tethering G6PD to vesicles. The α-syn C terminus is predicted to deposit into a pocket on the surface of the G6PD dimer, opposite the dimer interface (Figures 5A and 5B), where it is predicted to bind at the $NADP^+$ catalytic site and the G6P substrate binding site (Figure 5C). α-Syn fibrils, by contrast, are predicted to have multiple C-terminal tails simultaneously enter and bind the $NADP^+$ catalytic site and the G6P substrate binding sites on both G6PD dimer units (Figures 5D–5F). Indeed, fibrils phosphorylated at PS129 were predicted to enter farther into the G6PD binding pocket, even disrupting the $NADP^+$ structural site (Figure 5F). To confirm predictions that G6PD and α-syn bind directly, we performed isothermal titration calorimetry

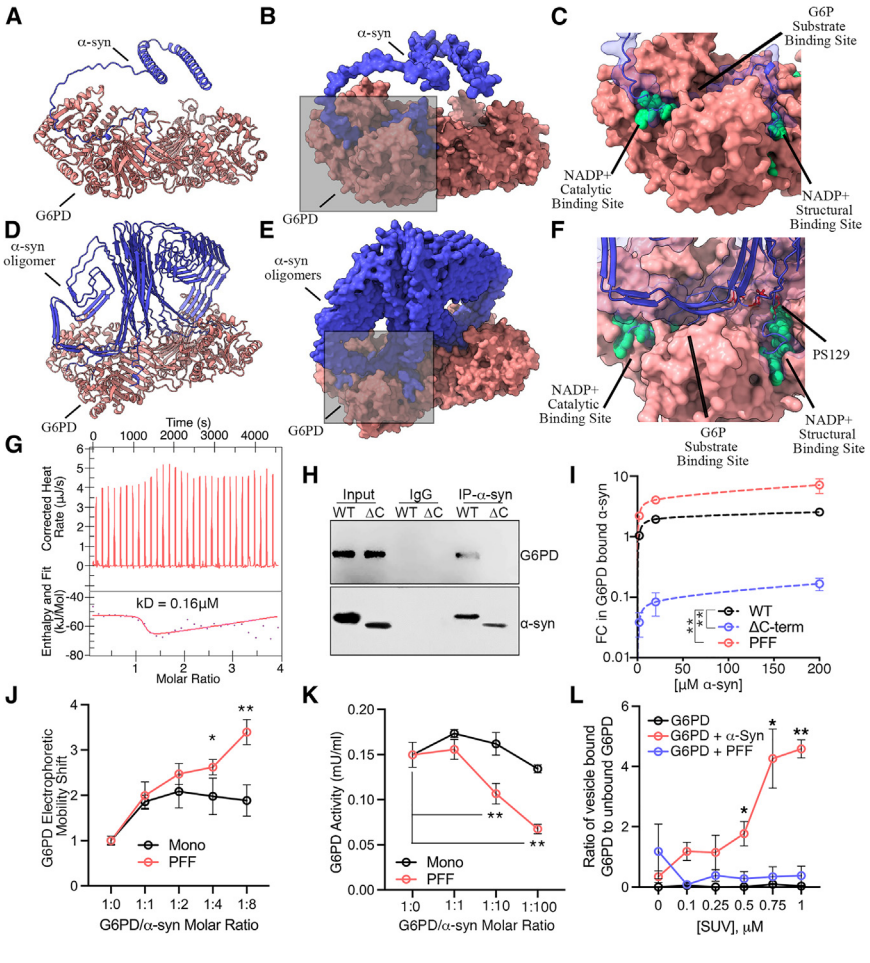

Figure 5. α-syn binds G6PD altering G6PD enzyme activity

(A–F) AlphaFold 3-mediated prediction of G6PD interaction with α-syn monomer (A–C) or fibrils (D–F) shows that the C terminus of α-syn binds to the catalytic and substrate pockets on the surface of G6PD opposite the dimer interface. Atomic (A and D) and surface (B and E) models are depicted, with an enlargement of the predicted interacting domain (C and F).

(G) ITC of G6PD and α-syn monomer interaction. Based on the ΔH and ΔG, the reaction is exothermic and spontaneous at the physiological temperature of 37°C. The curve suggests a model involving at least one binding site with a dissociation constant of 0.16 μM.

(H) α-syn pull-down assay shows that G6PD co-immunoprecipitates with full length α-syn but not α-syn-ΔC-term.

(I) Binding of increasing molar ratios of recombinant monomeric WT, α-syn-ΔC-term, or PFF-α-syn to G6PD (1:1, 10:1, 100:1) by slot blot ELISA. Kinetic data were fitted by non-linear regression and show significant differences in the apparent Kd (PFF < WT < ΔC-term). Data represent mean ± SEM. $n = 6$.

(J) Gel mobility shift assay of 4 μM G6PD with increasing molar ratios of either monomeric or PFF-α-syn. Data represent mean ± SEM. $n = 4$ replicate experiments. $^{*}p < 0.05$, $^{**}p < 0.01$ by ANOVA followed by post hoc Tukey test.

(K) Impact of increasing molar ratios of recombinant mono or PFF-α-syn on G6PD activity shows that PFF-α-syn dramatically decreases G6PD activity. Data represent mean ± SEM. $n = 6$, $^{**}p < 0.01$ by ANOVA followed by post hoc Tukey test.

(L) Binding of G6PD to 0.5 mM SUVs in the presence of increasing molar ratios of monomeric WT-α-syn, α-syn-ΔC-term, or PFF-α-syn was determined by flotation assay. Only WT-α-syn increases G6PD binding to SUVs. Data represent mean ± SEM. $n = 3$. $^{**}p < 0.01$ by ANOVA followed by post hoc Dunnett's test.

(ITC) with purified G6PD and α-syn (Figures 5G and S4A; Table S1). Injections of increasing molar ratios of α-syn into G6PD dimers equilibrated in the presence of both G6P and $NADP^+$ showed at least one α-syn binding site with a dissociation constant of 0.16 μM. This interaction was spontaneous and occurred at a 1:1 molar ratio. The role of the α-syn C terminus in this interaction was confirmed by immunoprecipitation, which showed co-immunoprecipitation of G6PD with full-length WT α-syn but not C-terminally truncated α-syn (ΔC-Term) (Figure 5H). Indeed, the binding kinetics of G6PD with increasing molar ratios of recombinant monomeric WT-α-syn, ΔC-Term-α-syn, or PFF-α-syn relative to G6PD (1:1, 10:1, and 100:1) by slot blot ELISA showed that ΔC-Term-α-syn has a significantly lower affinity for G6PD than WT-α-syn, which has a significantly lower affinity for G6PD than α-syn fibrils (PFFs) (Figure 5I). Increased binding of G6PD to α-syn fibrils (PFFs) relative to monomeric WT-α-syn was confirmed using electrophoretic mobility assays (Figures 5J and S4B–S4D). The upward mobility shift of G6PD in the presence of PFFs was significantly higher than that of monomeric α-syn at equimolar ratios and showed increased sedimentation into aggregates (Figure 5J; Figure S4D). This coincided with the inhibition of G6PD activity in response to PFFs, which occurred at a specific activity lower than that of α-syn monomers (Figures 5K and S4D). To determine whether the α-syn C terminus was important for G6PD incorporation into aggregates, we performed an aggregation assay, exposing SH-SY5Y cells expressing either WT-α-syn or ΔC-Term-α-syn to PFFs (Figures S4F and S4G). Immunolabeling of anti-aggregated α-syn and G6PD showed colocalization of G6PD with α-syn aggregates in WT-α-syn only, supporting the role of the α-syn C terminus in G6PD aggregation. Finally, we performed flotation assays to assess whether α-syn facilitated G6PD binding to small unilamellar vesicles (SUVs) (Figure 5L). Monomeric WT-α-syn increased the association of G6PD with SUVs relative to PFF-α-syn or G6PD alone, suggesting that α-syn binding to G6PD helps tether G6PD to synaptic vesicles. This led us to propose a model where the C terminus of α-syn, which remains flexible and exposed as part of the fibril assembly,[33] is sequestering G6PD into microaggregates and impeding G6PD activity. Collectively, these data support a role of α-syn in tethering

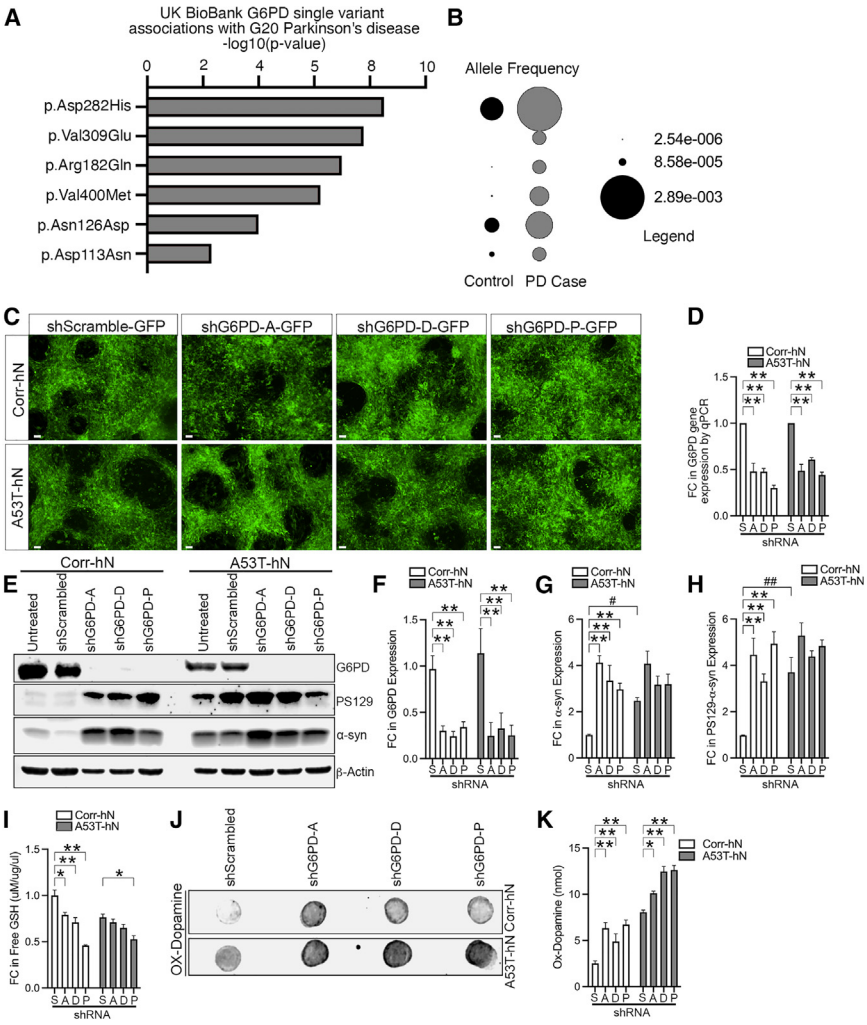

Figure 6. Loss of G6PD function is associated with PD onset

(A and B) Single-variant association analysis of G6PD missense mutations with an initial diagnosis of PD (G20) from 395,781 UK Biobank study participants showed several mutations with significant PD association. The allele frequency of each mutation in PD cases and controls is depicted (B).

(C and D) G6PD knockdown in hiPSC-derived A53T and corrected hNs (C) was confirmed by qPCR analysis of gene expression (D). Data represent mean ± SEM. $n = 6$. $^{**}p < 0.01$ by ANOVA followed by post hoc Dunnett's test. Scale bar: 50 μm.

(E–H) Western blot analysis in hiPSC-derived A53T and corrected hNs following G6PD knockdown (E) with quantification of G6PD (F), α-syn (G), and α-syn-PS129 (H) protein levels. Data represent mean ± SEM. $n = 4$. $^{**}p < 0.01$ by ANOVA followed by post hoc Dunnett's test. #$p < 0.05$ by Fisher least significant difference.

(I) GSH levels in in hiPSC-derived A53T and corrected hNs following G6PD knockdown. Data represent mean ± SEM. $n = 4$. $^{*}p < 0.05$, $^{**}p < 0.01$ by ANOVA followed by post hoc Dunnett's test.

(J–K) nIRF Ox-DA blots (J) with quantification (K). Data represent mean ± SEM. $n = 8$. $^{*}p < 0.05$, $^{**}p < 0.01$ by ANOVA followed by post hoc Dunnett's test. S, scrambled; A, shG6PD-A; D, shG6PD-D; P, shG6PD-pooled.

G6PD to synaptic vesicles and suggest that early α-syn aggregation impairs G6PD activity and disrupts redox balance.

Loss of G6PD function is a trigger for PD onset

We reasoned that, if impaired G6PD activity was an early causal event underlying DA loss in PD, then mutations in G6PD that impair activity and lead to G6PD deficiency syndrome should be associated with an increased risk of PD. We therefore used gene-based association summary statistics (GeneBass)[34] to access exome-based association statistics encompassing 4,529 phenotypes with gene-based and single-variant testing across 394,841 individuals with exome sequence data from the UK Biobank. Using GeneBass associations, we determined that G6PD variants have a significant gene burden association ($p = 0.0104$) with respect to an initial diagnosis of PD (G20 Parkinson's Disease, date of the first occurrence). We then looked at the missense mutations in G6PD with the strongest associations with PD (Figure 6A). The top 6 G6PD missense mutations with significant PD gene burden association all showed greater allele frequency in PD cases than controls (Figure 6B). Moreover, p.Asp282His, p.Arg182Gln, p.Asn126Asp, and p.Asp113Asn are clinically associated with pathogenic G6PD deficiency, as reported within the ClinVar database.[35,36] To confirm that loss of G6PD could phenoconvert control dopamine neurons to PD-like neurons, we silenced G6PD in hiPSC-derived corrected and A53T-hNs (Figures 6C–6K). Expression of GFP-tagged short hairpin RNA constructs against human G6PD resulted in a significant loss of G6PD gene expression (Figures 6C and 6D) coupled with robust silencing of G6PD protein (Figures 6E and 6F). Moreover, G6PD silencing resulted in a dramatic increase in total and PS129 α-syn levels, as seen by western blot analysis (Figures 6E, 6G, and 6H). To confirm that G6PD silencing perturbed redox homeostasis, we next assessed free GSH level and found GSH to be downregulated to levels comparable to those observed in A53T-hN in shG6PD-expressing corrected neurons (Figure 6I). G6PD silencing similarly resulted in increased Ox-DA adduct formation in shG6PD-expressing corrected neurons (Figures 6J and 6K). Collectively, these data strongly support a role of loss of G6PD enzyme activity in the initial loss of striatal DA and accumulation of pathological α-syn that lead to PD onset.

Restoring flux through the PPP rescues DA loss and prevents Ox-DA protein adduct formation

To determine whether restoring flux through the PPP could prevent or rescue the loss of DA in PD model systems, we took a multipronged approach where we intervened at several steps in the $NADPH^{+}/H^{+}$ and GSH cycles. We began by using NAC to restore

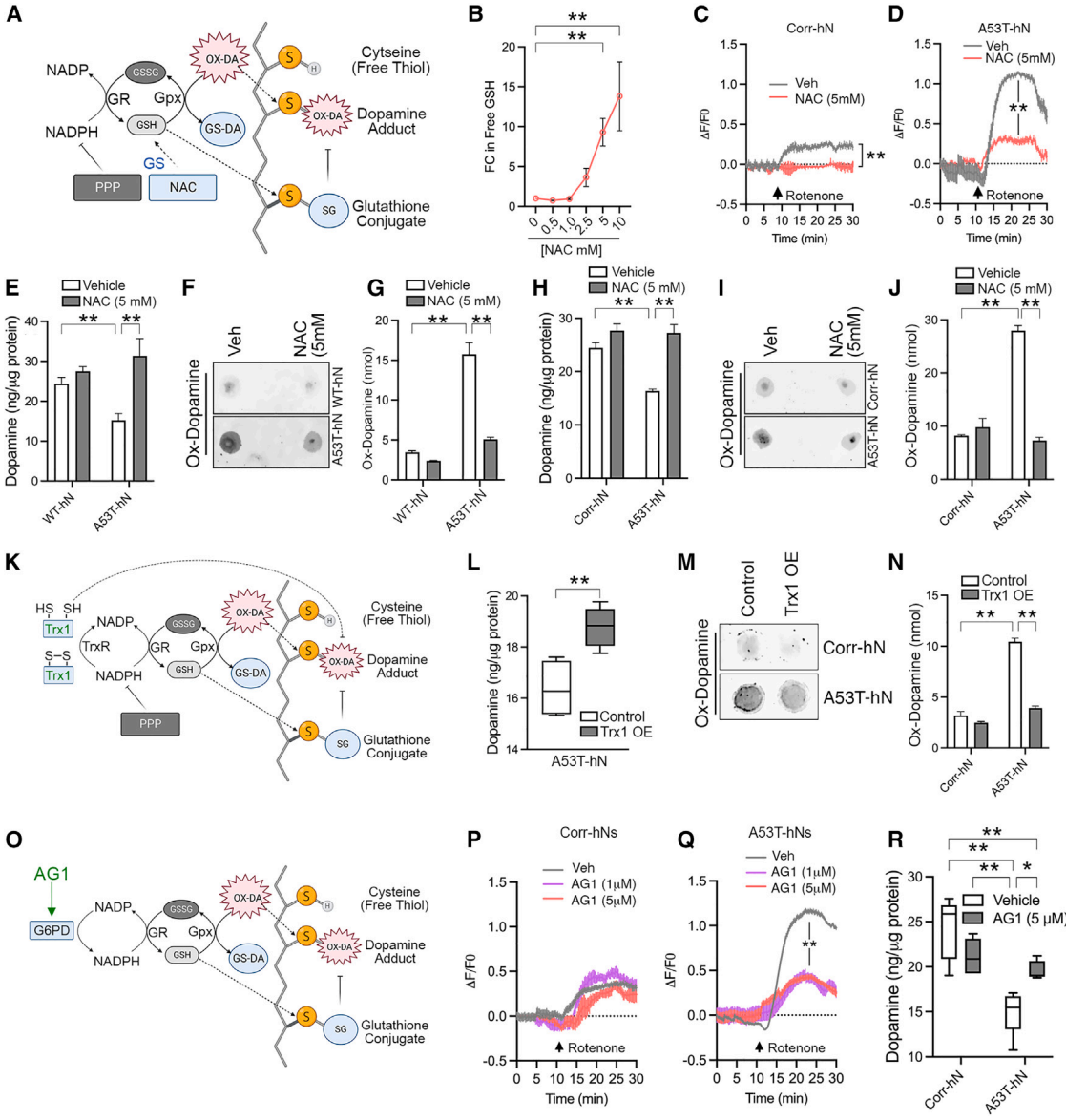

Figure 7. Modulating GSH synthesis rescues dopamine loss in α-syn mutant hNs

(A) Schematic of the NAC mode of action with respect to GSH cycling and reduction of DA adducts.

(B) Effect of NAC on levels of free GSH in cultured neurons. Data represent mean ± SEM. $n = 5$. $^{**}p < 0.01$ by ANOVA followed by post hoc Dunnett's test.

(C and D) Live imaging of the Grx1-roGFP (GSH/GSSG) sensor in corrected (Corr-hN) (C) or A53T-hNs (D) shows that NAC reduces rotenone-induced redox stress via GSH cycling.

(E–G) HPLC of total DA levels shows that NAC rescues DA loss in hESC-derived A53T-hNs (E) by reducing Ox-DA adduct formation (F), as quantified in (G). Data represent mean ± SEM. $n = 6$ independent cultures per condition over three differentiations. DIV: 45–55. $^{**}p < 0.01$ by ANOVA followed by post hoc Tukey test.

(H–J) HPLC of total DA levels shows that NAC rescues DA loss in hiPSC-derived A53T-hNs (H) by reducing Ox-DA adduct formation (I), as quantified in (J). Data represent mean ± SEM. $n = 6$ independent cultures per condition over three differentiations. DIV: 45–55. $^{**}p < 0.01$ by ANOVA followed by post hoc Tukey test.

(K) Schematic of the Trx mode of action from increasing NADPH and GSH cycling to reduction of DA-adducts.

(L–N) HPLC of total DA levels shows that Trx1 expression rescues DA loss in hiPSC-derived A53T-hNs (L) by reducing Ox-DA adduct formation (M), as quantified in (N). Data represent mean ± SEM. $n = 6$ independent cultures per condition over three differentiations. DIV: 45–55. $^{**}p < 0.01$ by ANOVA followed by post hoc Tukey test.

(O) Schematic of the AG1 mode of action by stabilizing G6PD and increasing G6PD activity, increasing GSH cycling and reduction of DA adducts.

(P–R) Live imaging of the Grx1-roGFP (GSH/GSSG) sensor in corrected (Corr-hN) (P) or A53T-hNs (Q) shows that AG1 reduces rotenone-induced redox stress via GSH cycling. HPLC of total DA levels shows that AG1 treatment rescues in DA loss in hiPSC-derived A53T-hNs (R). Data represent mean ± SEM. $n = 6$ independent cultures per condition over three differentiations. DIV: 45–55. $^{**}p < 0.01$ by ANOVA followed by post hoc Tukey test.

the ratio of GSH to GSSG in human PD neurons. NAC is deacetylated to cysteine after crossing the plasma membrane and provides cysteine as a substrate for glutamylation and subsequent GSH synthesis and is therefore one of the most direct means of increasing free cellular GSH (Figure 7A). NAC treatment of WT neurons resulted in a dose-dependent increase in free GSH levels within 24 h (Figure 7B). We therefore chose the lowest dose of NAC (5 mM) that had this effect in a 24-h period to test whether NAC treatment could restore GSH cycling in DA neurons harboring the A53T mutation (Figures 7C and 7D). Following 24 h of NAC exposure, we performed live imaging of GSH cycling using the redox-sensitive GSH probe GRX1-roGFP. GRX1 is a major redox enzyme that reduces disulfide bonds using GSH as an electron donor.[17] By linking this probe to a redox-sensitive GFP (roGFP), the probe senses changes in GSH oxidation state.[37] Live imaging of GRX1-roGFP control neurons (Figure 7C) showed that NAC significantly reduced GSH oxidation in response to rotenone. In A53T-hNs (Figure 7D), the baseline response to rotenone exposure was much higher than that observed in control neurons, and NAC treatment was able to reduce GSH oxidation to levels consistent with that observed in corrected control neurons (Figure 7D). These data collectively suggest that NAC treatment is able to raise free GSH levels to those consistent with a healthy control neuron. We next assessed whether normalized GSH levels translated into rescued DA levels. We measured the effect of NAC treatment on DA loss and Ox-DA protein adduct formation in both hESC-derived (Figures 7E–7G) and hiPSC-derived (Figures 7H–7J) PD neurons and their respective isogenic controls. NAC treatment for 24 h restored the loss of DA observed in both hESC-derived (Figure 7E) and hiPSC-derived (Figure 7H) A53T-hNs relative to the control. This translated into a reduction in Ox-DA protein adduct formation in both hESC-derived (Figure 7F and 7G) and hiPSC-derived (Figures 7I and 7J) PD systems. Collectively, these data show that intervention at the level of GSH cycling can restore DA loss resulting from α-syn microaggregate accumulation.

Since restoring GSH cycling reverses DA loss and oxidation, we next moved to enzyme-mediated restoration of redox balance. The thioredoxin system is an $NADPH^+/H^+$-dependent system comprising Trx, TrxR, and $NADPH^+/H^+$, which function collectively as a thiol reductase. Loss of $NADPH^+/H^+$ would result in accumulation of oxidized Trx and impairment in this system that would directly induce DA oxidation independent of GSH cycling (Figure 7K). Inducing Trx1 expression would increase thiol reduction capacity and has been independently reported to increase $NADPH^+/H^+$ synthesis through the PPP.[38] We therefore stably overexpressed Trx1 and assessed whether levels of total DA were increased and levels of Ox-DA adduct formation were decreased (Figures 7L–7N). HPLC analysis of total DA levels in hiPSC-derived A53T-hNs shows that Trx1 expression results in increased total DA relative to empty vector controls (Figure 7L). Moreover, near-infrared fluorescence (nIRF) analysis of Ox-DA protein adduct formation showed a corresponding decrease in Ox-DA-modified proteins (Figures 7M and 7N) in A53T-hNs, suggesting that the loss of DA was a direct result of increased DA oxidation.

In our final series of experiments, we set out to directly offset the deficit in G6PD activity with a small molecule that would offer higher translational potential. G6PD deficiency is one of the most common human genetic enzymopathies[39] and, as such, has been the target of significant investigation. High-throughput screening approaches have identified a small-molecule agonist, AG1,[40] that increases the activity of the WT G6PD as well as several common G6PD mutants (Figure 7O). We therefore, treated human DA neurons with AG1 to determine whether it increased PPP flux and subsequently normalized in-cell levels of DA in PD neurons. To determine whether AG1 treatment increased G6PD activity in the context of PD neurons, we performed a dose-response experiment of G6PD activation in PFF- and monomer-treated primary neurons (Figure S5). We found that AG1 increased G6PD activity in α-syn-PFF-exposed neurons to levels similar to those observed in α-syn-monomer-exposed cells at a range from 1 to 5 μM (Figure S5). We therefore tested the effects of 1 and 5 μM AG1 on GSH cycling by live imaging of Grx1-roGFP (Figures 7P and 7Q). AG1 had no significant effect on the ratio of GSH/GSSG in response to rotenone in control DA neurons (Figure 7P); however, in A53T neurons, AG1 significantly reduced GSH oxidation, indicating an increase in free GSH consistent with increased PPP activity (Figure 7Q). Our final experiment was performed to determine whether the increase in GSH that results from AG1 treatment correlated with increased total DA. Treatment of A53T-hNs with 5 μM AG1 significantly increased free DA levels relative to vehicle-treatment (Figure 7R). Collectively, these data identify the PPP as a targetable pathway in PD and suggest that small molecules that increase PPP flux, such AG1, may hold therapeutic potential.

DISCUSSION

The PPP coordinates both anabolic biosynthesis of nucleotides and redox homeostasis through ribose-5-phosphate and $NADPH^+/H^+$ synthesis, respectively. G6PD is the rate-limiting PPP enzyme that synthesizes $NADPH^+/H^+$ directly. G6PD expression, while ubiquitous, is highest in the brain,[41,42] as neurons preferentially metabolize glucose via the PPP to maintain redox homeostasis.[43] The elevated ATP requirements of fast-spiking nigral DA neurons puts them at risk of oxidative stress-induced injury and further necessitate redox buffering. This is achieved, in part, through the production of $NADPH^+/H^+$, which is needed to maintain the GSH cycle and regulate DA oxidation.[44–46] Here, we find that $NADPH^+/H^+$ and GSH levels are critical predictors of DA oxidation that results from α-syn microaggregate accumulation, consistent with the reported loss of $NADPH^+/H^+$ and GSH in postmortem PD brain tissue.[47] DA is a catechol consisting of a benzene ring with two hydroxyl (OH) groups attached to adjacent carbons. These hydroxyl groups are highly susceptible to oxidation, with DA-hydroxyl radicals giving rise to quinone formation. DA-quinones react with, and bind to, protein thiols, giving rise to DA-protein adducts that interfere with normal protein function. Analysis of dopamine, 3,4-dihydroxyphenylacetic acid (DOPAC), and dihydroxyphenylalanine oxidation to corresponding quinones in the brain of people with PD has shown a significant increase in the ratio of 5-*S*-cysteinyl-DA:DA and 5-*S*-cysteinyl-DOPAC:DOPAC in Parkinson groups relative to control groups.[48] This suggests that both metabolites are subject to oxidation in PD and may represent potential biomarkers of disease trajectory.

We report that PPP enzymes are tethered to synaptic vesicles, thereby providing localized redox buffering through the Trx/$NADPH^+/H^+$ system as well as through the GSH cycle. Vesicular tethering of metabolic enzymes has been reported for glycolytic enzymes, such as GAPDH, to provide localized ATP synthesis.[49,50] PPP enzymes have been reported in synaptosomal fractions, where enzyme activity is regulated by electrical stimulation.[51–53] Indeed, Huntingtin protein (HTT) was found to scaffold GAPDH to vesicles, and this tethering was lost in the context of mutant HTT, leading to neurodegeneration.[49] Under normal physiological conditions, α-syn localizes at high levels to the presynaptic regions of neurons, partitions between soluble[54] and lipid-associated forms,[55–58] and is likely involved in DA release[6,59] and in the maintenance of synaptic vesicle pools.[60,61] That HTT and α-syn undergo analogous processes with respect to the tethering of metabolic enzymes to vesicles is perhaps not surprising and may represent a common dysfunction that underlies multiple neurodegenerative diseases.

We also identify G6PD as a potential risk allele for PD. G6PD deficiency is a genetic disorder that affects red blood cells, leading to their vulnerability to oxidative stress and potential hemolytic anemia under certain conditions. Our analysis of datasets from the UK Biobank suggests a significant disease association between missense mutations in G6PD and initial diagnosis of PD. Indeed, postmortem analysis of PD putamen and cerebellum have reported reduced G6PD expression in both brain regions,[47] and we find G6PD deposition in LBs within the putamen of PD brain sections. We also find that loss of G6PD phenocopies the accumulation of pathological α-syn and loss of DA associated with PD onset. This effect, while surprising, is likely due to the reported oxidative regulation of casein kinase 2 (CK2). CK2 is a primary regulator of α-syn phosphorylation.[62] In addition, CK2 phospho-activates G6PD at T145 in response to stress in order to maintain redox homeostasis.[63] In the absence of G6PD, reactive nitrogen species activate CK2 through S-nitrosylation,[64] resulting in increased α-syn phosphorylation at S129, impairing protein turnover.[64] Furthermore, G6PD-overexpressing mice that show a moderate increase in G6PD activity, are rendered resistant to the toxic effects of 1-methyl-4-phenyl-1,2,3,6-tetrahydropyridine, suggesting that expression of G6PD in DA neurons is neuroprotective against PD-related stressors.[65] Moreover, these data suggest that loss of G6PD activity, specifically in nigral DA neurons, may convey susceptibility to environmental exposure predicted to trigger PD through redox stress-associated mechanisms.[24,66]

Biochemical experiments indicated that the activation of G6PD by AG1 is noncovalent and that G6PD homodimer ligand function requires homodimer formation.[67] Missense mutations result in various clinical phenotypes depending on the nature and location of the mutation. Mutations may lie in the catalytic domain and reduce activity without abolishing it.[68] By contrast, mutations disrupting the homodimer interface of G6PD have notable pathological effects, as the stability and catalytic activity of G6PD primarily rely on its oligomerization to dimeric and tetrameric forms.[68,69] As the catalytic domain spans the dimer interface, monomers per se are inactive.[70] AG1 is also a dimer that promotes G6PD dimer formation and stabilization in a dose-dependent manner.[67] While we predict that α-syn binds opposite the dimer interface, phosphorylated α-syn fibrils are predicted to enter the $NADP^+$ structural binding site that is important for dimer stabilization. It is therefore, interesting to speculate as to whether G6PD binding to α-syn microaggregates disrupts G6PD dimer formation, whereas α-syn monomers may tether G6PD dimers and/or tetramers. This would explain why AG1 had a greater effect on G6PD activity in A53T-mutant hNs than their genome-corrected counterparts, and the ligand may maintain the G6PD dimer in the face of the opposing influence of α-syn microaggregates.

There is currently a lack of therapeutic options available to those affected by PD that correct the early loss of DA and block DA oxidation. NAC is a membrane-permeable form of cysteine and a precursor for GSH. Many animal models of PD have shown that NAC administration rescues dopaminergic neuron loss, reduces oxidative stress, and improves motor outcomes.[71–74] Indeed, we find that NAC is an effective tool with respect to rescuing DA loss and reducing Ox-DA protein adduct formation. Clinical trials have investigated the effectiveness of NAC and demonstrate that oral coupled with intravenous administration of NAC increases the expression of the dopamine transporter and modestly improves Unified Parkinson's Disease Rating Scale scores in people with PD.[75,76] However, NAC has low oral bioavailability, and repeated intravenous administration is needed to maintain an active dose. Therefore, future endeavors to rescue early DA loss in PD should focus on alternative approaches to activating the PPP and maintaining the $NADPH^+/H^+$ and GSH cycles. Activation of the Trx/$NADPH^+/H^+$ system as well as maintaining G6PD activity with AG1-related molecules may offer new advances regarding this long-standing issue.

Limitations of the study

A decrease in both PPP and glycolytic flux can also result from downstream tricarboxylic acid (TCA) cycle defects that may impact flux through both the PPP and glycolysis by slowing metabolic flux without lowering the maximum rate of G6PD activity. Indeed, this mechanism has been reported in synucleinopathy models, where aberrantly S-nitrosylated TCA cycle enzymes, principally α-ketoglutarate dehydrogenase/succinyl coenzyme-A synthetase, slow metabolic activity.[77] S-nitrosylated TCA enzymes have been observed in the human LBD brain, suggesting pathophysiological relevance.[77] While we observed G6PD deposition in LBs of the PD brain and PFF-exposed animals, the effect in animals was variable, suggesting that multiple comorbidities may combine to promote G6PD deposition in LB deposits.

RESOURCE AVAILABILITY

Lead contact

Requests for further information, resources, and reagents should be directed to and will be fulfilled by the lead contact, Scott D. Ryan (scott.ryan@ucalgary.ca).

Materials availability

This study did not generate new or unique reagents.

Data and code availability

- All metabolomics data have been deposited at MetaboLights:www.ebi.ac.uk/metabolights/MTBLS11250) and are publicly available as of the date of publication. The accession number is MTBLS11250.
- This paper does not report original code.

- Any additional information required to reanalyze the data reported in this paper is available from the lead contact upon request. All requests for raw and analyzed data and materials are reviewed by the University of Calgary to verify whether the request is subject to any intellectual property or confidentiality obligations. Patient-related data not included in the paper may be subject to patient confidentiality. Any data and materials that can be shared will be released via a materials transfer agreement. All other generated or analyzed data in this study are included in this published article (and its supplemental information files).

ACKNOWLEDGMENTS

This work was supported in part by the Canadian Institutes of Health Research (2014 and 2021 to S.D.R.), the Natural Sciences and Engineering Research Council of Canada (RG060805 to S.D.R.), and the Vanier Program (to M.G.S.). We thank Dr. Andrew Boyce, Yannick Fouad, and Dr. Roger Thompsons for sharing material and expertise related to caspase-3 analysis of neurodegeneration. We acknowledge the following core facilities that supported this work: Charbonneau Microscopy, Toronto SickKids Imaging Facility, Alberta Precision Laboratories, and the Calgary Metabolomics Research Facility.

AUTHOR CONTRIBUTIONS

S.D.R. was responsible for project oversight and design. M.G.S. conducted experimental work and analyses related to cell culture, microscopy, and protein fractionation and analysis experiments with the assistance of C.L.C. and S.V.S. P.L., S.C., and G.B.F. performed protein structure and biochemical analysis. R.P. and O.H.-G. oversaw ITC experiments and analysis. J.T.J. facilitated neuropathology analysis and interpretation. E.-K.A. performed image analysis with the assistance of E.T. M.G.S. and E. Soubeyrand performed dopamine analysis with the assistance of T.A.A. R.W.L.S. and E. Stuart performed *in vivo* studies under the guidance of J.C.W. M.G.S. and S.D.R. prepared and edited the manuscript with the assistance of J.C.W. and E.T.

DECLARATION OF INTERESTS

The authors declare no competing interests.

STAR★METHODS

Detailed methods are provided in the online version of this paper and include the following:

SUPPLEMENTAL INFORMATION

Supplemental information can be found online at https://doi.org/10.1016/j.celrep.2024.115178.

Received: September 14, 2024
Revised: November 20, 2024
Accepted: December 18, 2024
Published: January 7, 2025

REFERENCES

1. Burke, R.E., and O'Malley, K. (2013). Axon degeneration in Parkinson's disease. Exp. Neurol. *246*, 72–83.
2. Fearnley, J.M., and Lees, A.J. (1991). Ageing and Parkinson's disease: substantia nigra regional selectivity. Brain *114*, 2283–2301.
3. Riederer, P., and Wuketich, S. (1976). Time course of nigrostriatal degeneration in parkinson's disease. A detailed study of influential factors in human brain amine analysis. J. Neural. Transm. *38*, 277–301.
4. Spira, P.J., Sharpe, D.M., Halliday, G., Cavanagh, J., and Nicholson, G.A. (2001). Clinical and pathological features of a Parkinsonian syndrome in a family with an Ala53Thr alpha-synuclein mutation. Ann. Neurol. *49*, 313–319.
5. Martin, L.J., Semenkow, S., Hanaford, A., and Wong, M. (2014). Mitochondrial permeability transition pore regulates Parkinson's disease development in mutant alpha-synuclein transgenic mice. Neurobiol. Aging *35*, 1132–1152.
6. Chandra, S., Gallardo, G., Fernández-Chacón, R., Schlüter, O.M., and Südhof, T.C. (2005). Alpha-synuclein cooperates with CSPalpha in preventing neurodegeneration. Cell *123*, 383–396.
7. Volpicelli-Daley, L.A., Luk, K.C., and Lee, V.M.Y. (2014). Addition of exogenous alpha-synuclein preformed fibrils to primary neuronal cultures to seed recruitment of endogenous alpha-synuclein to Lewy body and Lewy neurite-like aggregates. Nat. Protoc. *9*, 2135–2146.
8. Luk, K.C., Kehm, V., Carroll, J., Zhang, B., O'Brien, P., Trojanowski, J.Q., and Lee, V.M.Y. (2012). Pathological alpha-synuclein transmission initiates Parkinson-like neurodegeneration in nontransgenic mice. Science *338*, 949–953.
9. Hallam, R.D., Buchner-Duby, B., Stykel, M.G., Coackley, C.L., and Ryan, S.D. (2022). Intracellular Accumulation of alpha-Synuclein Aggregates Promotes S-Nitrosylation of MAP1A Leading to Decreased NMDAR-Evoked Calcium Influx and Loss of Mature Synaptic Spines. J. Neurosci. *42*, 9473–9487.
10. Zarranz, J.J., Alegre, J., Gómez-Esteban, J.C., Lezcano, E., Ros, R., Ampuero, I., Vidal, L., Hoenicka, J., Rodriguez, O., Atarés, B., et al. (2004). The new mutation, E46K, of alpha-synuclein causes Parkinson and Lewy body dementia. Ann. Neurol. *55*, 164–173.
11. Guzman, J.N., Sanchez-Padilla, J., Wokosin, D., Kondapalli, J., Ilijic, E., Schumacker, P.T., and Surmeier, D.J. (2010). Oxidant stress evoked by pacemaking in dopaminergic neurons is attenuated by DJ-1. Nature *468*, 696–700.
12. Mosharov, E.V., Larsen, K.E., Kanter, E., Phillips, K.A., Wilson, K., Schmitz, Y., Krantz, D.E., Kobayashi, K., Edwards, R.H., and Sulzer, D. (2009). Interplay between cytosolic dopamine, calcium, and alpha-synuclein causes selective death of substantia nigra neurons. Neuron *62*, 218–229.
13. Beal, M.F. (2001). Experimental models of Parkinson's disease. Nat. Rev. Neurosci. *2*, 325–334.
14. Lipton, S.A., and Rosenberg, P.A. (1994). Excitatory amino acids as a final common pathway for neurologic disorders. N. Engl. J. Med. *330*, 613–622.

15. Lipton, S.A. (2006). Paradigm shift in neuroprotection by NMDA receptor blockade: memantine and beyond. Nat. Rev. Drug Discov. *5*, 160–170.

16. Stykel, M.G., and Ryan, S.D. (2024). Network analysis of S-nitrosylated synaptic proteins demonstrates unique roles in health and disease. Biochim. Biophys. Acta Mol. Cell Res. *1871*, 119720.

17. Stykel, M.G., and Ryan, S.D. (2022). Nitrosative stress in Parkinson's disease. NPJ Parkinsons Dis. *8*, 104.

18. Schildknecht, S., Gerding, H.R., Karreman, C., Drescher, M., Lashuel, H.A., Outeiro, T.F., Di Monte, D.A., and Leist, M. (2013). Oxidative and nitrative alpha-synuclein modifications and proteostatic stress: implications for disease mechanisms and interventions in synucleinopathies. J. Neurochem. *125*, 491–511.

19. Danielson, S.R., Held, J.M., Schilling, B., Oo, M., Gibson, B.W., and Andersen, J.K. (2009). Preferentially increased nitration of α-synuclein at tyrosine-39 in a cellular oxidative model of Parkinson's disease. Anal. Chem. *81*, 7823–7828.

20. Paxinou, E., Chen, Q., Weisse, M., Giasson, B.I., Norris, E.H., Rueter, S.M., Trojanowski, J.Q., Lee, V.M., and Ischiropoulos, H. (2001). Induction of α-synuclein aggregation by intracellular nitrative insult. J. Neurosci. *21*, 8053–8061.

21. Souza, J.M., Giasson, B.I., Chen, Q., Lee, V.M., and Ischiropoulos, H. (2000). Dityrosine cross-linking promotes formation of stable α-synuclein polymers: implication of nitrative and oxidative stress in the pathogenesis of neurodegenerative synucleinopathies. J. Biol. Chem. *275*, 18344–18349.

22. Giasson, B.I., Duda, J.E., Murray, I.V., Chen, Q., Souza, J.M., Hurtig, H.I., Ischiropoulos, H., Trojanowski, J.Q., and Lee, V.M. (2000). Oxidative damage linked to neurodegeneration by selective α-synuclein nitration in synucleinopathy lesions. Science *290*, 985–989.

23. Soldner, F., Laganière, J., Cheng, A.W., Hockemeyer, D., Gao, Q., Alagappan, R., Khurana, V., Golbe, L.I., Myers, R.H., Lindquist, S., et al. (2011). Generation of isogenic pluripotent stem cells differing exclusively at two early onset Parkinson point mutations. Cell *146*, 318–331.

24. Ryan, S.D., Dolatabadi, N., Chan, S.F., Zhang, X., Akhtar, M.W., Parker, J., Soldner, F., Sunico, C.R., Nagar, S., Talantova, M., et al. (2013). Isogenic human iPSC Parkinson's model shows nitrosative stress-induced dysfunction in MEF2-PGC1α transcription. Cell *155*, 1351–1364.

25. Czaniecki, C., Ryan, T., Stykel, M.G., Drolet, J., Heide, J., Hallam, R., Wood, S., Coackley, C., Sherriff, K., Bailey, C.D.C., and Ryan, S.D. (2019). Axonal pathology in hPSC-based models of Parkinson's disease results from loss of Nrf2 transcriptional activity at the Map1b gene locus. Proc. Natl. Acad. Sci. USA *116*, 14280–14289.

26. Kouroupi, G., Taoufik, E., Vlachos, I.S., Tsioras, K., Antoniou, N., Papastefanaki, F., Chroni-Tzartou, D., Wrasidlo, W., Bohl, D., Stellas, D., et al. (2017). Defective synaptic connectivity and axonal neuropathology in a human iPSC-based model of familial Parkinson's disease. Proc. Natl. Acad. Sci. USA *114*, E3679–E3688.

27. Fujiwara, H., Hasegawa, M., Dohmae, N., Kawashima, A., Masliah, E., Goldberg, M.S., Shen, J., Takio, K., and Iwatsubo, T. (2002). alpha-Synuclein is phosphorylated in synucleinopathy lesions. Nat. Cell Biol. *4*, 160–164.

28. Walker, D.G., Lue, L.F., Adler, C.H., Shill, H.A., Caviness, J.N., Sabbagh, M.N., Akiyama, H., Serrano, G.E., Sue, L.I., and Beach, T.G.; Arizona Parkinson Disease Consortium (2013). Changes in properties of serine 129 phosphorylated alpha-synuclein with progression of Lewy-type histopathology in human brains. Exp. Neurol. *240*, 190–204.

29. Gilles, J.F., Dos Santos, M., Boudier, T., Bolte, S., and Heck, N. (2017). DiAna, an ImageJ tool for object-based 3D co-localization and distance analysis. Methods *115*, 55–64.

30. Luk, K.C., Kehm, V.M., Zhang, B., O'Brien, P., Trojanowski, J.Q., and Lee, V.M.Y. (2012). Intracerebral inoculation of pathological alpha-synuclein initiates a rapidly progressive neurodegenerative alpha-synucleinopathy in mice. J. Exp. Med. *209*, 975–986.

31. Tran, H.T., Chung, C.H.Y., Iba, M., Zhang, B., Trojanowski, J.Q., Luk, K.C., and Lee, V.M.Y. (2014). A-synuclein immunotherapy blocks uptake and templated propagation of misfolded alpha-synuclein and neurodegeneration. Cell Rep. *7*, 2054–2065.

32. Lau, A., So, R.W.L., Lau, H.H.C., Sang, J.C., Ruiz-Riquelme, A., Fleck, S.C., Stuart, E., Menon, S., Visanji, N.P., Meisl, G., et al. (2020). α-Synuclein strains target distinct brain regions and cell types. Nat. Neurosci. *23*, 21–31.

33. Medeiros, J., Bamm, V.V., Jany, C., Coackley, C., Ward, M.E., Harauz, G., Ryan, S.D., and Ladizhansky, V. (2021). Partial magic angle spinning NMR ^{1}H, ^{13}C, ^{15}N resonance assignments of the flexible regions of a monomeric alpha-synuclein: conformation of C-terminus in the lipid-bound and amyloid fibril states. Biomol. NMR Assign. *15*, 297–303.

34. Karczewski, K.J., Solomonson, M., Chao, K.R., Goodrich, J.K., Tiao, G., Lu, W., Riley-Gillis, B.M., Tsai, E.A., Kim, H.I., Zheng, X., et al. (2022). Systematic single-variant and gene-based association testing of thousands of phenotypes in 394,841 UK Biobank exomes. Cell Genom. *2*, 100168.

35. Landrum, M.J., Lee, J.M., Benson, M., Brown, G., Chao, C., Chitipiralla, S., Gu, B., Hart, J., Hoffman, D., Hoover, J., et al. (2016). ClinVar: public archive of interpretations of clinically relevant variants. Nucleic Acids Res. *44*, D862–D868.

36. Landrum, M.J., Chitipiralla, S., Brown, G.R., Chen, C., Gu, B., Hart, J., Hoffman, D., Jang, W., Kaur, K., Liu, C., et al. (2020). ClinVar: improvements to accessing data. Nucleic Acids Res. *48*, D835–D844.

37. Gutscher, M., Pauleau, A.L., Marty, L., Brach, T., Wabnitz, G.H., Samstag, Y., Meyer, A.J., and Dick, T.P. (2008). Real-time imaging of the intracellular glutathione redox potential. Nat. Methods *5*, 553–559.

38. Wang, X., Wang, Z., Wu, J., Wang, L., Li, X., Shen, H., Li, H., Xu, J., Li, W., and Chen, G. (2022). Thioredoxin 1 regulates the pentose phosphate pathway via ATM phosphorylation after experimental subarachnoid hemorrhage in rats. Brain Res. Bull. *185*, 162–173.

39. Howes, R.E., Piel, F.B., Patil, A.P., Nyangiri, O.A., Gething, P.W., Dewi, M., Hogg, M.M., Battle, K.E., Padilla, C.D., Baird, J.K., and Hay, S.I. (2012). G6PD deficiency prevalence and estimates of affected populations in malaria endemic countries: a geostatistical model-based map. PLoS Med. *9*, e1001339.

40. Hwang, S., Mruk, K., Rahighi, S., Raub, A.G., Chen, C.H., Dorn, L.E., Horikoshi, N., Wakatsuki, S., Chen, J.K., and Mochly-Rosen, D. (2018). Correcting glucose-6-phosphate dehydrogenase deficiency with a small-molecule activator. Nat. Commun. *9*, 4045.

41. Morellini, M., Colonna-Romano, S., Meloni, T., Battistuzzi, G., and Gandini, E. (1985). Glucose-6-phosphate dehydrogenase of leukocyte subpopulations in normal and enzyme deficient individuals. Haematologica *70*, 390–395.

42. Battistuzzi, G., D'Urso, M., Toniolo, D., Persico, G.M., and Luzzatto, L. (1985). Tissue-specific levels of human glucose-6-phosphate dehydrogenase correlate with methylation of specific sites at the 3' end of the gene. Proc. Natl. Acad. Sci. USA *82*, 1465–1469.

43. Herrero-Mendez, A., Almeida, A., Fernández, E., Maestre, C., Moncada, S., and Bolaños, J.P. (2009). The bioenergetic and antioxidant status of neurons is controlled by continuous degradation of a key glycolytic enzyme by APC/C-Cdh1. Nat. Cell Biol. *11*, 747–752.

44. Drukarch, B., Jongenelen, C.A., Schepens, E., Langeveld, C.H., and Stoof, J.C. (1996). Glutathione is involved in the granular storage of dopamine in rat PC 12 pheochromocytoma cells: implications for the pathogenesis of Parkinson's disease. J. Neurosci. *16*, 6038–6045.

45. Satoh, T., and Lipton, S.A. (2007). Redox regulation of neuronal survival mediated by electrophilic compounds. Trends Neurosci. *30*, 37–45.

46. Wu, D.C., Teismann, P., Tieu, K., Vila, M., Jackson-Lewis, V., Ischiropoulos, H., and Przedborski, S. (2003). NADPH oxidase mediates oxidative stress in the 1-methyl-4-phenyl-1,2,3,6-tetrahydropyridine model of Parkinson's disease. Proc. Natl. Acad. Sci. USA *100*, 6145–6150.

47. Toulorge, D., Schapira, A.H.V., and Hajj, R. (2016). Molecular changes in the postmortem parkinsonian brain. J. Neurochem. *139*, 27–58.

48. Fornstedt Wallin, B. (2024). Oxidation of dopamine and related catechols in dopaminergic brain regions in Parkinson's disease and during ageing in non-Parkinsonian subjects. J. Neural. Transm. *131*, 213–228.

49. Zala, D., Hinckelmann, M.V., Yu, H., Lyra da Cunha, M.M., Liot, G., Cordelières, F.P., Marco, S., and Saudou, F. (2013). Vesicular glycolysis provides on-board energy for fast axonal transport. Cell *152*, 479–491.

50. Hinckelmann, M.V., Virlogeux, A., Niehage, C., Poujol, C., Choquet, D., Hoflack, B., Zala, D., and Saudou, F. (2016). Self-propelling vesicles define glycolysis as the minimal energy machinery for neuronal transport. Nat. Commun. *7*, 13233.

51. Roy, D., and Singh, R. (1983). Age-related changes in glucose-6-phosphate dehydrogenase and 6-phosphogluconate dehydrogenase in the subcellular fractions from the rat brain and the effect of dimethylaminoethanol. Biochem. Int. *7*, 43–53.

52. Kimura, H., Naito, K., Nakagawa, K., and Kuriyama, K. (1974). Activation of hexose monophosphate pathway in brain by electrical stimulation in vitro. J. Neurochem. *23*, 79–84.

53. Kauffman, F.C., and Harkonen, M.H. (1977). Metabolites and enzymes of the pentose phosphate pathway in isolated nerve endings. J. Neurochem. *28*, 745–750.

54. Theillet, F.X., Binolfi, A., Bekei, B., Martorana, A., Rose, H.M., Stuiver, M., Verzini, S., Lorenz, D., van Rossum, M., Goldfarb, D., and Selenko, P. (2016). Structural disorder of monomeric alpha-synuclein persists in mammalian cells. Nature *530*, 45–50.

55. Iwai, A., Masliah, E., Yoshimoto, M., Ge, N., Flanagan, L., de Silva, H.A., Kittel, A., and Saitoh, T. (1995). The precursor protein of non-A beta component of Alzheimer's disease amyloid is a presynaptic protein of the central nervous system. Neuron *14*, 467–475.

56. Maroteaux, L., Campanelli, J.T., and Scheller, R.H. (1988). Synuclein: a neuron-specific protein localized to the nucleus and presynaptic nerve terminal. J. Neurosci. *8*, 2804–2815.

57. Jensen, P.H., Nielsen, M.S., Jakes, R., Dotti, C.G., and Goedert, M. (1998). Binding of alpha-synuclein to brain vesicles is abolished by familial Parkinson's disease mutation. J. Biol. Chem. *273*, 26292–26294.

58. Bussell, R., Jr., and Eliezer, D. (2004). Effects of Parkinson's disease-linked mutations on the structure of lipid-associated alpha-synuclein. Biochemistry *43*, 4810–4818.

59. Burré, J., Sharma, M., Tsetsenis, T., Buchman, V., Etherton, M.R., and Sudhof, T.C. (2010). Alpha-synuclein promotes SNARE-complex assembly in vivo and in vitro. Science *329*, 1663–1667.

60. Murphy, D.D., Rueter, S.M., Trojanowski, J.Q., and Lee, V.M. (2000). Synucleins are developmentally expressed, and alpha-synuclein regulates the size of the presynaptic vesicular pool in primary hippocampal neurons. J. Neurosci. *20*, 3214–3220.

61. Abeliovich, A., Schmitz, Y., Fariñas, I., Choi-Lundberg, D., Ho, W.H., Castillo, P.E., Shinsky, N., Verdugo, J.M., Armanini, M., Ryan, A., et al. (2000). Mice lacking alpha-synuclein display functional deficits in the nigrostriatal dopamine system. Neuron *25*, 239–252.

62. Okochi, M., Walter, J., Koyama, A., Nakajo, S., Baba, M., Iwatsubo, T., Meijer, L., Kahle, P.J., and Haass, C. (2000). Constitutive phosphorylation of the Parkinson's disease associated alpha-synuclein. J. Biol. Chem. *275*, 390–397.

63. Hao, Y., Ren, T., Huang, X., Li, M., Lee, J.H., Chen, Q., Liu, R., and Tang, Q. (2023). Rapid phosphorylation of glucose-6-phosphate dehydrogenase by casein kinase 2 sustains redox homeostasis under ionizing radiation. Redox Biol. *65*, 102810.

64. Wu, W., Sung, C.C., Yu, P., Li, J., and Chung, K.K.K. (2020). Correction: S-Nitrosylation of G protein-coupled receptor kinase 6 and Casein kinase 2 alpha modulates their kinase activity toward alpha-synuclein phosphorylation in an animal model of Parkinson's disease. PLoS One *15*, e0235296.

65. Mejías, R., Villadiego, J., Pintado, C.O., Vime, P.J., Gao, L., Toledo-Aral, J.J., Echevarría, M., and López-Barneo, J. (2006). Neuroprotection by transgenic expression of glucose-6-phosphate dehydrogenase in dopaminergic nigrostriatal neurons of mice. J. Neurosci. *26*, 4500–4508.

66. Pezzoli, G., and Cereda, E. (2013). Exposure to pesticides or solvents and risk of Parkinson disease. Neurology *80*, 2035–2041.

67. Raub, A.G., Hwang, S., Horikoshi, N., Cunningham, A.D., Rahighi, S., Wakatsuki, S., and Mochly-Rosen, D. (2019). Small-Molecule Activators of Glucose-6-phosphate Dehydrogenase (G6PD) Bridging the Dimer Interface. ChemMedChem *14*, 1321–1324.

68. Cunningham, A.D., Colavin, A., Huang, K.C., and Mochly-Rosen, D. (2017). Coupling between Protein Stability and Catalytic Activity Determines Pathogenicity of G6PD Variants. Cell Rep. *18*, 2592–2599.

69. Cunningham, A.D., and Mochly-Rosen, D. (2017). Structural analysis of clinically relevant pathogenic G6PD variants reveals the importance of tetramerization for G6PD activity. Matters (Zur) *2017*.

70. Garcia, A.A., Mathews, I.I., Horikoshi, N., Matsui, T., Kaur, M., Wakatsuki, S., and Mochly-Rosen, D. (2022). Stabilization of glucose-6-phosphate dehydrogenase oligomers enhances catalytic activity and stability of clinical variants. J. Biol. Chem. *298*, 101610.

71. Munoz, A.M., Rey, P., Soto-Otero, R., Guerra, M.J., and Labandeira-Garcia, J.L. (2004). Systemic administration of N-acetylcysteine protects dopaminergic neurons against 6-hydroxydopamine-induced degeneration. J. Neurosci. Res. *76*, 551–562.

72. Clark, J., Clore, E.L., Zheng, K., Adame, A., Masliah, E., and Simon, D.K. (2010). Oral N-acetyl-cysteine attenuates loss of dopaminergic terminals in alpha-synuclein overexpressing mice. PLoS One *5*, e12333.

73. Berman, A.E., Chan, W.Y., Brennan, A.M., Reyes, R.C., Adler, B.L., Suh, S.W., Kauppinen, T.M., Edling, Y., and Swanson, R.A. (2011). N-acetylcysteine prevents loss of dopaminergic neurons in the EAAC1-/- mouse. Ann. Neurol. *69*, 509–520.

74. Ghosh, S., Won, S.J., Wang, J., Fong, R., Butler, N.J.M., Moss, A., Wong, C., Pan, J., Sanchez, J., Huynh, A., et al. (2021). α-synuclein aggregates induce c-Abl activation and dopaminergic neuronal loss by a feed-forward redox stress mechanism. Prog. Neurobiol. *202*, 102070.

75. Monti, D.A., Zabrecky, G., Kremens, D., Liang, T.W., Wintering, N.A., Cai, J., Wei, X., Bazzan, A.J., Zhong, L., Bowen, B., et al. (2016). N-Acetyl Cysteine May Support Dopamine Neurons in Parkinson's Disease: Preliminary Clinical and Cell Line Data. PLoS One *11*, e0157602.

76. Monti, D.A., Zabrecky, G., Kremens, D., Liang, T.W., Wintering, N.A., Bazzan, A.J., Zhong, L., Bowens, B.K., Chervoneva, I., Intenzo, C., and Newberg, A.B. (2019). N-Acetyl Cysteine Is Associated With Dopaminergic Improvement in Parkinson's Disease. Clin. Pharmacol. Ther. *106*, 884–890.

77. Doulias, P.T., Yang, H., Andreyev, A.Y., Dolatabadi, N., Scott, H., K Raspur, C., Patel, P.R., Nakamura, T., Tannenbaum, S.R., Ischiropoulos, H., and Lipton, S.A. (2023). S-Nitrosylation-mediated dysfunction of TCA cycle enzymes in synucleinopathy studied in postmortem human brains and hiPSC-derived neurons. Cell Chem. Biol. *30*, 965–975.e6.

78. Kriks, S., Shim, J.W., Piao, J., Ganat, Y.M., Wakeman, D.R., Xie, Z., Carrillo-Reid, L., Auyeung, G., Antonacci, C., Buch, A., et al. (2011). Dopamine neurons derived from human ES cells efficiently engraft in animal models of Parkinson's disease. Nature *480*, 547–551.

79. Giasson, B.I., Duda, J.E., Quinn, S.M., Zhang, B., Trojanowski, J.Q., and Lee, V.M.Y. (2002). Neuronal alpha-synucleinopathy with severe movement disorder in mice expressing A53T human alpha-synuclein. Neuron *34*, 521–533.

80. Gómez-Manzo, S., Terrón-Hernández, J., de la Mora-de la Mora, I., García-Torres, I., López-Velázquez, G., Reyes-Vivas, H., and Oria-Hernández, J. (2013). Cloning, expression, purification and characterization of his-tagged human glucose-6-phosphate dehydrogenase: a simplified method for protein yield. Protein J. *32*, 585–592.

81. Volpicelli-Daley, L.A., Luk, K.C., Patel, T.P., Tanik, S.A., Riddle, D.M., Stieber, A., Meaney, D.F., Trojanowski, J.Q., and Lee, V.M.Y. (2011). Exogenous alpha-synuclein fibrils induce Lewy body pathology leading to synaptic dysfunction and neuron death. Neuron *72*, 57–71.

82. Gulyássy, P., Puska, G., Györffy, B.A., Todorov-Völgyi, K., Juhász, G., Drahos, L., and Kékesi, K.A. (2020). Proteomic comparison of different synaptosome preparation procedures. Amino Acids *52*, 1529–1543.

83. Liu, C., Goel, P., and Kaeser, P.S. (2021). Spatial and temporal scales of dopamine transmission. Nat. Rev. Neurosci. *22*, 345–358.

84. Lu, W., Clasquin, M.F., Melamud, E., Amador-Noguez, D., Caudy, A.A., and Rabinowitz, J.D. (2010). Metabolomic analysis via reversed-phase ion-pairing liquid chromatography coupled to a stand alone orbitrap mass spectrometer. Anal. Chem. *82*, 3212–3221.

85. Melamud, E., Vastag, L., and Rabinowitz, J.D. (2010). Metabolomic analysis and visualization engine for LC-MS data. Anal. Chem. *82*, 9818–9826.

86. Clasquin, M.F., Melamud, E., and Rabinowitz, J.D. (2012). LC-MS data processing with MAVEN: a metabolomic analysis and visualization engine. Curr Protoc Bioinformatics. *14*, Unit.14. 11.

87. De Benedetto, G.E., Fico, D., Pennetta, A., Malitesta, C., Nicolardi, G., Lofrumento, D.D., De Nuccio, F., and La Pesa, V. (2014). A rapid and simple method for the determination of 3,4-dihydroxyphenylacetic acid, norepinephrine, dopamine, and serotonin in mouse brain homogenate by HPLC with fluorimetric detection. J. Pharm. Biomed. Anal. *98*, 266–270.

88. Burbulla, L.F., Song, P., Mazzulli, J.R., Zampese, E., Wong, Y.C., Jeon, S., Santos, D.P., Blanz, J., Obermaier, C.D., Strojny, C., et al. (2017). Dopamine oxidation mediates mitochondrial and lysosomal dysfunction in Parkinson's disease. Science *357*, 1255–1261.

89. Mazzulli, J.R., Burbulla, L.F., Krainc, D., and Ischiropoulos, H. (2016). Detection of Free and Protein-Bound ortho-Quinones by Near-Infrared Fluorescence. Anal. Chem. *88*, 2399–2405.

90. Mirdita, M., Schütze, K., Moriwaki, Y., Heo, L., Ovchinnikov, S., and Steinegger, M. (2022). ColabFold: making protein folding accessible to all. Nat. Methods *19*, 679–682.

91. Jumper, J., Evans, R., Pritzel, A., Green, T., Figurnov, M., Ronneberger, O., Tunyasuvunakool, K., Bates, R., Žídek, A., Potapenko, A., et al. (2021). Highly accurate protein structure prediction with AlphaFold. Nature *596*, 583–589.

92. Mayer, L.D., Hope, M.J., and Cullis, P.R. (1986). Vesicles of variable sizes produced by a rapid extrusion procedure. Biochim. Biophys. Acta *858*, 161–168.

93. Antón, Z., Landajuela, A., Hervás, J.H., Montes, L.R., Hernández-Tiedra, S., Velasco, G., Goñi, F.M., and Alonso, A. (2016). Human Atg8-cardiolipin interactions in mitophagy: Specific properties of LC3B, GABARAPL2 and GABARAP. Autophagy *12*, 2386–2403.

STAR★METHODS

KEY RESOURCES TABLE

REAGENT or RESOURCE	SOURCE	IDENTIFIER
Antibodies		
Donkey anti-Rabbit IgG (H&L) Secondary Antibody, Alexa Fluor 488	Life Technologies (Invitrogen)	Cat# A21206; RRID:AB_2535792
Donkey anti-Mouse IgG (H&L) Secondary Antibody, Alexa Fluor 488 conjugate	Life Technologies (Invitrogen)	Cat# A21202; RRID:AB_141607
Donkey anti-Rabbit IgG (H&L) Secondary Antibody, Alexa Fluor 555	Life Technologies (Invitrogen)	Cat# A32794; RRID:AB_2762834
Donkey anti-Mouse IgG (H&L) Secondary Antibody, Alexa Fluor 555 conjugate	Life Technologies (Invitrogen)	Cat# A32773; RRID: AB_276284
Donkey anti-Rabbit IgG (H&L) Secondary Antibody, Alexa Fluor 647	Life Technologies (Invitrogen)	Cat# A32795; RRID: AB_2762835
Donkey anti-Mouse IgG (H&L) Secondary Antibody, Alexa Fluor 647 conjugate	Life Technologies (Invitrogen)	Cat# A32787; RRID:AB_2762830
anti-mouse IgG	Santa cruz	sc-3877; RRID: AB_737222
anti-rabbit IgG	Abcam	ab172730, RRID: AB_2687931
Anti-Phosphoserine-129 (81A)/Purified anti-α-Synuclein Phospho (Ser129) Antibody (Previously Covance catalog# MMS-5091) mouse monoclonal	Biolegend	Cat# 825701; RRID# AB_2734593
total Anti-a-synuclein/a-Synuclein antibody monoclonal mouse	BD	Cat# 610787; RRID:AB_398108
Anti-TH/TH (Tyrosine Hydroxylase) antibody polyclonal rabbit	Pel-Freeze	Cat# P40101; RRID:AB_2313713
anti-α-syn (PS129)/Recombinant Anti-Alpha-synuclein (Phosphor S129) antibody [EP1536Y]	Abcam	Cat# ab51253; RRID:AB_869973
Goat anti-Mouse IgG (H + L) Secondary Antibody, HRP	Thermo Fisher Scientific	Cat# 31430; RRID:AB_228307
Goat anti-Rabbit IgG (H + L) Secondary Antibody, HRP	Thermo Fisher Scientific	Cat# 31460; RRID:AB_228341
Rabbit anti-Chicken IgY (H + L) Secondary Antibody, HRP	Thermo Fisher Scientific	Cat# 31401; RRID:AB_228385
anti-mouse (800) Li-Cor infrared conjugated secondary/IRDye 800CW Donkey anti-Mouse IgG antibody	LI-COR Biosciences	Cat# 926–32212; RRID:AB_621847
Anti rabbit (700) Li-Cor infrared conjugated secondary/IRDye 680RD Donkey anti-Rabbit IgG antibody	LI-COR Biosciences	Cat# 926–68073; RRID:AB_10954442
Rab7 (D95F2) XP/Rab7 antibody	CELL SIGNALING	Cat# 9367; RRID:AB_1904103
EEA1 antibody [EPR4245] mono rabbit	Abcam	Cat# ab109110; RRID:AB_10863524
Cox IV antibody mono mouse	Abcam	Cat# ab14744; RRID:AB_301443
Synaptophysin 1 antibody poly chicken	SY SY	Cat#101006; RRID:AB_2622239
PSD95 antibody mono mouse	SY SY	Cat#124011; RRID:AB_2619799
Beta-Actin antibody mono mouse	Sigma-Aldrich	Cat# A5441; RRID:AB_476744
G6PD Antibody poly rabbit	Invitrogen	Cat# PA5-29662; RRID:AB_2547137
G6PD Antibody poly rabbit	Invitrogen	Cat# PA5-25017; RRID:AB_2542517
G6PD Antibody mono mouse	ProteinTech	Cat# 66373-1; RRID:AB_2877122
PGLS Antibody poly rabbit	Invitrogen	Cat# PA5-98053; RRID:AB_2812667

(*Continued on next page*)

Continued

REAGENT or RESOURCE	SOURCE	IDENTIFIER
PGLS Antibody mono rabbit	Invitrogen	Cat# ab129199; RRID:AB_11144133
PGD Antibody poly rabbit	Invitrogen	Cat# PA5-80894; RRID:AB_2788158
Cyclin B1 Antibody mono rabbit	Abcam	Cat# ab32053; RRID:AB_731779
Cyclin B1 Antibody poly rabbit	Cell Signaling	Cat# 4138; RRID:AB_2072132
MSI 2 Antibody mono rabbit	Abcam	Cat# ab76148; RRID:AB_1523981
DAPI (4′,6-Diamidino-2-Phenylindole)	Invitrogen	Cat# D1306
Bacterial and virus strains		
E. coli BL21-CodonPlus (DE3)-RIPL competent cells	Agilent	Cat# 230280
Biological samples		
Human Striatal Brain Blocks	Calgary Brain Bank	https://hbi.ucalgary.ca/calgary-brain-bank/home
Chemicals, Peptides, and Recombinant Proteins		
AG-1	MedChem Express	Cat# HY-123962
Rotenone	Sigma	Cat# R8875
N-acetyl-l-cysteine	Sigma	Cat# A9165
LDN193189 HYDROCHLORIDE, ≥98% (HPLC)	Sigma	Cat# SML0559
SB431542	Sigma	Cat# S4317
Sonic Hedgehog (SHH) C25II	R&D	Cat#464-SH-025
Purmorphamine	Tocris	Cat#4551
Fibroblast growth factor 8/Recombinant Human/Murine FGF-8b	Peprotech	Cat# 100-25
CHIR99021 ≥ 98% (HPLC)	Sigma	Cat# SML1046
Brain Derived Neurotrophic Factor/ Recombinant Human/Murine/Rat BDNF	Peprotech	Cat#450-02
ascorbic acid/L-Ascorbic acid powder, suitable for cell culture, γ-irradiated	Sigma	Cat# A8960
Glial Derived Neurotrophic Factor/ Recombinant Human GDNF	Peprotech	Cat# 450-10
transforming growth factor β 3/Recombinant Human TGF-β3	Peprotech	Cat# 100-36E
dibutyryl cAMP/N^6,2′-*O*-Dibutyryladenosine 3′,5′-cyclic monophosphate sodium salt ≥96% (HPLC), powder	Sigma	Cat# D0627
DAPT	Biogems/Peprotech	Cat# 2088055
poly-ornithine/Poly-L-ornithine solution mol wt 30,000–70,000, 0.01%, sterile-filtered, BioReagent, suitable for cell culture	Sigma	Cat# P4957
Laminin/Corning™ Laminin, Mouse	Fisher/Corning	Cat# C354232
Fibronectin/Corning™ Fibronectin, Human	Fisher/Corning	Cat# C354008
PFA/32% Paraformaldehyde (formaldehyde) aqueous solution	Electron Microscopy Sciences	Cat#15714
PBS	Sigma	Cat# D8537
BSA	Bioshop	Cat# ALB001.100
Triton X-100	Sigma	Cat# X100
Glutaraldehyde solution, 25% in H_2O	Sigma	Cat# 49626
Sodium azide ReagentPlus®, ≥99.5%	Sigma	Cat# S2002
Sodium Chloride (Crystalline/Certified ACS), Fisher Chemical™	Fisher	Cat# S271

(*Continued on next page*)

Continued

REAGENT or RESOURCE	SOURCE	IDENTIFIER
Urea	Fisher	Cat# PI29700
Sodium Dodecyl Sulfate (SDS), White Powder, Electrophoresis, Fisher BioReagents™	Fisher	Cat# BP166
NaF/Sodium Fluoride (Powder/Certified ACS), Fisher Chemical™	Fisher	Cat#S299100
PMSF/Phenylmethanesulfonyl fluoride ≥98.5% (GC)	Sigma	Cat# P7626
NaV/Sodium orthovanadate, 99%	Fisher/ACROS Organics	Cat# 205330500
Aprotinin	Bioshop	APR600.25
Sucrose/D-Sucrose (Molecular Biology), Fisher BioReagents	Fisher	Cat# FLBP220212
Imidazole/Imidazole (Molecular Biology), Fisher BioReagents™	Fisher	Cat# BP305-50
EDTA/Ethylenediaminetetraacetic Acid, Disodium Salt Dihydrate (Crystalline/Certified ACS), Fisher Chemical™	Fisher	Cat# S311
Cycloheximide/Cycloheximide, High Purity - CAS 66-81-9 - Calbiochem	Sigma	Cat#239764
Clarity Western ECL Substrate	Bio-Rad	Cat# 1705061
IPTG/Isopropyl β-D-1-thiogalactopyranoside	Bioshop	Cat# IPT002.25
LB media	Sigma	Cat#L3522
Ampicilline, Sodium Salt - CAS 69-52-3 - Calbiochem	Sigma	Cat# 171254
5X Reducing Sample Buffer/Thermo Scientific™ Pierce™ Lane Marker Reducing Sample Buffer	Fisher	Cat#PI39000
mTeSR™ PlusComplete Kit	STEMCELL Technologies Inc	Cat# 100-0276
ReLeSR™ passaging reagent	STEMCELL Technologies Inc	Cat# 100-0484
Accutase solution	Sigma	Cat# A6964
Matrigel/Corning™ Matrigel™ hESC-Qualified Matrix	Fisher/Corning	Cat# 08-774-552
KSR/Gibco™ KnockOut™ Serum Replacement	Fisher/Gibco	Cat#10828010
B27/Gibco™ B-27™ Supplement (50X), serum free	Fisher/Gibco	Cat#17504044
Gibco™ *N*-2 Supplement (100X)	Fisher/Gibco	Cat# 17502048
DMEM/Dulbecco's Modified Eagle's Medium/Nutrient Mixture F-12 Ham With L-glutamine, 15 mM HEPES, and sodium bicarbonate, liquid, sterile-filtered, suitable for cell culture	Sigma	Cat#D8437
Gibco Antibiotic-Antimycotic (100X)	Fisher	Cat# 15240062
Gibco Bovine Albumin Fraction V (7.5% solution)	Fisher	Cat# 15260037
Gibco β-mercaptoethanol	Fisher	Cat# 21985023
Fetal Bovine Serum (FBS)/FBS Optima	R&D Systems	Cat# S12450
HyClone™ Non-Essential Amino Acids (NEAA) 100X	Fisher	Cat# SH3023801
Gibco Penicillin-Streptomycin (10,000 U/mL)/Pen Strep	Fisher	Cat# 15-140-122
Gibco 100mM Sodium Pyruvate Solution	Fisher	Cat# 11360070

(*Continued on next page*)

Continued

REAGENT or RESOURCE	SOURCE	IDENTIFIER
Gelatin/Gelatin from bovine skin	Sigma	Cat# G9391
G6PD Recombinant	R&D Systems	Cat# 10096-DH
Dopamine hydrochloride Standard	Sigma	Cat# 1225204
Doxycycline hyclate	Sigma	Cat# D9891
HiSpeed Maxi Plasmid kit	Qiagen	Cat# 12662
Opti-MEM	Fisher	Cat# 31985-062
Polyethyleneimine (PEI transfection reagent)	Santacruz	Cat# sc-507213
Polyethylene Glycol 8000 (PEG), Fisher BioReagents	Fisher	BP233-1
Nucleospin RNA Virus	Takara Bio	Cat# 740956.10
Lenti-X qRT-PCR Titration Kit	Takara Bio	Cat# 631235
Quantitect Reverse Transcription kit	Qiagen	Cat# 205311
SsoAdvanced Universal SYBR® Green Supermix	BioRad	Cat# 1725270
Dynabeads protein G	Invitrogen	Cat#10004D
Critical Commercial Assays		
Bio-Rad DC Protein assay	Bio-Rad	Cat#5000112
G6PD activity assay	Abcam	Cat# ab176722
Glutathione Colorimetric Detection Kit	Invitrogen	Cat# EIAGSHC
Fluorometric NADP/NADPH Assay Kit	Abcam	Cat# ab176724
Deposited Data		
Metabolomic Data	Metabolights	Metabolights:MTBLS11250
Experimental Models: Cell Lines		
Human: hESC-derived WT and A53T cell lines	Gifted from Rudolf Jaenisch, Whitehead Inst, MIT, Boston, MA	N/A
Human: hiPSC-derived Corrected and A53T cell lines	Gifted from Rudolf Jaenisch, Whitehead Inst, MIT, Boston, MA	N/A
Human: SHSY5Y cells	ATCC	Cat# CRL-2266
Experimental models: Organisms/strains		
Mouse: B6C3F1/J	The Jackson Laboratory	Jax: 100010
Mouse: B6; C3-Tg(Prnp-SNCA*A53T)83Vle/J	The Jackson Laboratory	Jax: 004479
Oligonucleotides		
G6PD forward	Sigma	AGCTGGAGGACTTCTTTGCC
G6PD reverse	Sigma	TGATGCGGTTCCAGCCTATC
Recombinant DNA		
pET21a-alpha-synuclein	Addgene	Cat#51486
pET21a-alpha-synuclein-delta-C-Term (a.a. 1–119)	Genscript	Custom
pET28a+-G6PD-Sumo	Genscript	Custom
pWPXLd_EF1a_Trx1_IRES_EGFP	Genscript	Custom
pWPXLd backbone	Addgene	12258
pLenti6.2_mCherry_Grx1_roGFP2	Addgene	155045
shScramble-GFP	Origene	TR30021
shG6PD-A-GFP	Origene	TL312877A - ATGAGCCAGATAGGCTGG AACCGCATCAT
shG6PD-D-GFP	Origene	TL312877D - CAGCCGTCGTCCTCTATG TGGAGAATGAG

(*Continued on next page*)

Continued

REAGENT or RESOURCE	SOURCE	IDENTIFIER
Software and Algorithms		
Axio-observer Zen Pro software	Zeiss	https://www.zeiss.com/microscopy/int/products/microscope-software/zen.html
ImageJ	National Institute of Health	https://imagej.nih.gov/ij/download.html
Image Studio Software For Li-Cor Odyssey Fc	LI-COR	https://www.licor.com/bio/image-studio/
FPLC DuoLogic system	Bio-Rad	N/A Discontinued system
HPLC Waters system Millennium 32 software	Waters	N/A
Prism7	Graphpad Software Inc	https://www.graphpad.com/scientific-software/prism/
MAVEN	Open-source	http://maven.princeton.edu
NanoAnalyze (V3.0)	TA Instruments	https://www.tainstruments.com/sw/nano_analyze.html
AlphaFold3	DeepMind	https://alphafoldserver.com/welcome

EXPERIMENTAL MODEL AND STUDY PARTICIPANT DETAILS

hiPSC/hESC culture and A9 DA neuronal differentiation

hiPSC isogenic lines (Female) and hESC isogenic lines (Male) were generated as described by.[23] Genotypes of hESC-derived WT and A53T as well as hiPSC-derived Corrected and A53T cell lines were confirmed by restriction digest of genomic DNA.[23] hPSCs were cultured as previously described[24] with slight modifications. Briefly, pluripotent cells were plated in mTeSR Plus (Stem Cell Technologies) and media was changed daily. The colonies were passed weekly with ReLeSR (Stem Cell Technologies). Differentiation of hPSCs into A9-type DA neurons was performed by following a floor plate differentiation paradigm.[24,78] Immediately preceding differentiation, the colonies were dissociated into a single cell suspension using Accutase. hPSCs were collected and re-plated at $4x10^4$ cells/cm^2 on Matrigel (BD)-coated tissue culture dishes for differentiation. Floor-plate induction was carried out using hESC-medium containing knockout serum replacement (KSR), LDN193189 (100 nM), SB431542 (10 μM), Sonic Hedgehog (SHH) C25II (100 ng/mL, Purmorphamine (2 μM), Fibroblast growth factor 8 (FGF8; 100 ng/mL), and CHIR99021 (3 μM). On day 5 of differentiation, KSR medium was incrementally shifted to N2 medium (25%, 50%, 75%) every 2 days. On day 11, the medium was changed to Neurobasal/B27/Glutamax supplemented with CHIR. On day 13, CHIR was replaced with Brain-Derived Neurotrophic Factor (BDNF; 20 ng/mL), ascorbic acid (0.2 mM), Glial Derived Neurotrophic Factor (GDNF; 20 ng/mL), transforming growth factor β 3 (TGFβ3; 1 ng/mL), dibutyryl cAMP (dbcAMP; 0.5 mM), and DAPT (10 μM) for 9 days. On day 20, cells were dissociated using Accutase and re-plated under high cell density $4x10^5$ cells/cm^2 in terminal differentiation medium (NB/B27 + BDNF, ascorbic acid, GDNF, dbcAMP, TGFβ3 and DAPT) also referred to as DA Neuron (DAN)-Medium, on dishes pre-coated with polyornithine (15 μg/mL)/laminin (1 μg/mL)/fibronectin (2 μg/mL). Cells were differentiated for up to 60 DIV, with analysis performed at DIV 45 and/or DIV 60.

PFF inoculated mice

Homozygous M83 transgenic mice ($M83^{+/+}$), which express A53T-mutant human α-synuclein under the control of the mouse prion protein promoter[79] on a mixed C57BL6/C3H background, and B6C3F1 non-transgenic mice were purchased from The Jackson Laboratories (stock numbers 004479 and 100010, respectively). These two lines were intercrossed to generate hemizygous TgM83 mice, which were housed at four to five animals per cage. Mice were maintained on a 12 h light–12 h dark cycle and were given unlimited access to food and water. All mouse experiments were performed in accordance with guidelines set by the Canadian Council on Animal Care and approved by the University Health Network Animal Care Committee (protocol #4623.17). Inoculations were performed as follows: Male, 37-day-old hemizygous M83 mice were anesthetized with isoflurane and then inoculated non-stereotactically using a tuberculin syringe with an attached 27 gauge, 0.5-inch needle (BD Biosciences, 305945) with 30 μL of sample at a depth of ~3 mm into the right cerebral hemisphere. This region corresponds to the hippocampus or thalamus. For inoculations with recombinant α-synuclein preparations (monomeric or PFF), each mouse received 2 μg of total α-synuclein diluted in inoculum diluent buffer (5% (w/v) BSA prepared in sterile PBS). Mice were euthanized at either 90- or 120-day post-inoculation. Brains were divided parasagittally and either flash frozen for protein and GSH analysis, placed in Tissue Storage Solution (130-100-008, MACS) for fresh tissue isolation of SVs and NADPH analysis, or perfused and fixed with paraformaldehyde for immunohistochemistry.

Rat primary neurons culture

Primary cortical neurons were harvested from both male and female E18 Sprague-Dawley rat embryos (Charles River). Following dissection, pooled tissue was digested using filter-sterilized 17U/mg Papain (Sigma, P4762) solution and subjected to mechanical

dissociation. Cells were seeded onto plates coated the previous day (0.15 mg/mL Poly-D-Lysine hydrobromide (Sigma, P0899) in sterile tissue culture grade water at 37°C for 24 h) and incubated at 37°C, 7.5% CO2 until time of analysis. Alternating every 4 and 3 days, a 50% media change was performed using fresh primary culture media [(2% B27 supplement (Gibco, 17504044), 1% antibiotic/antimycotic (Gibco, 15240062), 0.7% BSA Fraction V (Gibco, 15260037), 0.1% β-mercaptoethanol (Gibco, 21985-023) in DMEM/F12 (Sigma, D8437)]. If required, at day 7, *in vitro* cells were treated with 1 μg/mL human α-syn pre-formed fibrils (PFFs), 1 μg/mL monomeric α-syn, or vehicle control (PBS) as previously described.[9]

SHSY5Y culture and differentiation

SHSY5Y-cells (Female) stably expressing WT-α-syn or ΔC-Term-α-syn were maintained in growth media [MEM-1% nonessential amino acids (HyClone SH30238.01), 1% pen/strep (GIBCO, 15140122), 1% sodium pyruvate (GIBCO 11360-070) containing 15% fetal bovine serum (R&D S12450)]. Cells were plated onto gelatin-coated coverslips in a 24-well plate and treated with 1ug/ml human α-syn pre-formed fibrils (PFFs) for 72hrs prior to fixation and immunocytochemistry.

Human tissue Procurement and analysis

Formalin-fixed, paraffin-embedded brain sections of cognitively normal and Parkinson's Disease cases with confirmed Lewy Body deposition were obtained from the Calgary Brain Bank. 4–6 μm-thick sections of putamen from sporadic PD and non-PD controls (death from cancer or myocardial infarction) were examined with by standard immunohistochemical techniques. Age and sex were not disclosed. Histology was performed by Alberta Precision Laboratories using total αsyn (ms) BD Bioscience 610787 at 1:300, with secondary HRP magenta chromogen and G6PD (ms) Proteintech 66373-1 at 1:50, with secondary DAB HRP substrate.

METHOD DETAILS

Purification of recombinant proteins and formation of human α-syn preformed fibrils

G6PD with N-terminal 6his-SUMO tag was custom cloned into a pET28a+ (GenScript, USA). Human G6PD and α-syn protein were isolated from BL21-CodonPlus (DE3)-RIPL competent cells (Agilent, 230280) transformed with either pET21a-alpha-synuclein (Addgene, 51486) or pET28a+-G6PD-SUMO. α-syn was purified by sequential ion-exchange FPLC and reversed-phase HPLC. Purification of G6PD-SUMO was performed by ammonium sulfate precipitation[80] followed by affinity chromatography-FPLC using a pre-equilibrated (20mM Tris, 300 mM NaCl, pH: 7.4) 5mL Nickel column (EconoFit Nuvia IMAC Column, Bio-Rad) at 4°C G6PD-SUMO was eluted (20mM Tris, 300 mM NaCl, 250 mM Imidazole, pH: 7.4) and buffer exchanged (20mM Tris, 150 mM NaCl, pH: 7.4) and the SUMO-tag was cleaved using 2 μg/mg of SUMO-protease with 2 mM Dithiothreitol (DTT). Affinity chromatography was repeated to capture the SUMO-tag and purified G6PD was eluted. Human α-syn PFFs were generated as previously described.[81] Purified α-syn (5 mg/mL in PBS) was incubated at 37°C with constant shaking for 7 days, then aliquoted and stored at −80°C. Prior to use, PFFs were thawed and diluted in PBS, then subjected to sonication (20% amplitude, 30 s; 1 s on, 1 s off) to ensure a fibril size between 50 and 100μM, and added to neuronal media for exposure to neurons at a concentration of 1 μg/mL. Both fibrillar and monomeric α-syn were analyzed by sedimentation assay to confirm the separation of monomers from fibrils prior to use. For *in vivo* experiments in heterozygous M83 mice, untagged full-length recombinant WT human α-syn was expressed and purified as previously described.[32] To generate PFFs, α-syn was incubated at 1 mg/mL concentration in 20 mM Tris-HCl pH 7.4 and 100 mM NaCl with shaking at 600 rpm on an Eppendorf Thermomixer F1.5 for 10 days at 37°C, then aliquoted and stored at −80°C. Prior to inoculation into mice, PFFs were thawed at room temperature and transferred into 0.2 mL thin-walled PCR tubes, then subjected to sonication (70% amplitude, 4 cycles of 15 s on and 2 min rest) in a QSonica Q700 sonicator.

Lentiviral expression for G6PD shRNA knockdown and Grx1_roGFP2 imaging

pWPXLd_EF1a_Trx1_IRES_EGFP, was generated by cloning of the Trx1 ORF into the pWPXLd backbone (Addgene #12258). pWPXLd_EF1a_Trx1_IRES_EGFP or pLenti6.2_mCherry_Grx1_roGFP2 (Addgene #155045) were maxi-prepped (Qiagen 12662) and sequences confirmed by Sanger-sequencing (AAC Genomics Facility, University of Guelph). For shRNA-mediated knockdown of G6PD, two unique 29-mer sequences targeting human G6PD mRNA and a 29-mer non-effective scrambled shRNA cassette, were commercially designed by Origene in the pGFP-C-shLenti vector (TL312877) and maxi-prepped (Qiagen 12662) for lentivirus generation. Lenti-293T cells were cultured until 70% confluency and transfected with packaging plasmid (psPAX2; Addgene #12260), envelop plasmid (pMD2.G; Addgene #12253) and the target plasmid, using a polyethyenimine (PEI) transfection protocol. Viral titer was determined using the Takara Lenti-X qRT-PCR titration kit according to the manufacturer's protocol (Takara 631235). After viral collection, the virus was concentrated using concentration buffer (40%w/v PEG8000, 1.2M NaCl and 1% PBS final pH7.0–7.2) by adding 3:1 viral supernatant:concentrator volume and incubating overnight at 4°C with shaking. Thereafter, the virus/concentrator was centrifuged at 1600g for 60 min at 4°C. The supernatant was decanted, and viral pellet resuspended in PBS, aliquoted and stored at −80°C. For viral transduction, hPSCs grown in 10cm plate format were infected at day 10 of differentiation by adding virus (MOI 30) in 5mL N2 media. After 6 h, transduction media was removed and replaced with fresh N2 media, and the differentiation protocol continued. For live imaging of Grx1_roGFP2, cells were imaged with an Axio-observer Live-cell imaging microscope with LED-based illumination and Optical Sectioning by structured illumination (Zeiss). Objectives used were Plan-APO 40x/1.4 Oil DIC (UV) VIS-IR or Plan-APO 63x/1.4 Oil DIC M27. Fluorescence intensity was measured with the analysis module of Zen 3.4 (Zeiss).

Immunocytochemistry and fluorescence analysis

Cells were fixed with 4% PFA for 5 min, washed 3x with PBS, permeabilized and blocked with 3% BSA and 0.3% Triton X-100 in PBS for 1hr. Cells were incubated with primary antibody overnight and the appropriate AlexaFluor (488, 555, 647) conjugated secondary antibodies were used at a dilution of 1:2000. Primary antibodies and dilutions were as follows: Anti-Phosphoserine-129 (81A) (ms) (1:10,000) BioLegend, anti-TH (rb) (1:1000) from Pelfreeze, anti-synaptophysin (chk) (1:1000) from SYSY and anti-G6PD (rb) (1:500) from Invitrogen PA5-25017. Monomeric or PFF inoculated mice were cryosectioned, and immunohistochemistry was performed using the same protocol and antibody dilutions as described. Imaging was performed using a Zeiss LSM with Airyscan Fast with approx. 110nm (XY) and 400nm (Z) resolution, or Zeiss Elyra PS with approx. 100 nm (XY) and 300 nm (Z) resolution, equipped with 405 nm (150 mW), 488 nm (200 mW), 561 nm (200 mW) and 640 nm (150 mW) lasers and an Andor iXon3 885 (SIM). Distance analysis was performed using the DiAna module of ImageJ 2.9.0, while intensity measurements were performed using the object recognition tool of Volocity 6.3 (PerkinElmer). DiANA is performed on individual punctae and averaged across all datasets (coverslips or animals).

Subcellular protein fractionations

Rodent and human SVs were isolated or enriched from synaptosomal preparations derived using an adaptation of established methods.[82] Briefly, cells or tissue were washed with PBS and resuspended in homogenization buffer (250 mM sucrose, 3 mM imidazole,1 mM EDTA, 0.03 mM cycloheximide) and dounced 40X with tight/B pestle. The nuclear pellet and cell debris were removed by centrifugation (1000 x g 5 min at 4°C). The supernatant (S2) was removed from the resulting pellet (VMP) and transferred to a new tube. In the case of human DA neurons, which form vesicular hot spots rather than classic synapses,[83] the synaptosome fraction is minimal, and the resulting supernatant (S2) contains the majority of SVs. In the case of rodent brain and primary rat neuron culture, where true synaptosomes do form, synaptosome fractions were further isolated from the VMP (which contains crude vesicle, mitochondria, and synaptosomes) by resuspending the pellet in 1mL homogenization buffer and layered on top of a sucrose gradient (5mL of 0.8M sucrose over 5mL 1.2M sucrose). Samples were spun at 54,000g for 90 mins at 4°C. The cloudy band at 0.8M/1.2M interface (approx. 1.5mL) was collected via syringe with an 18G needle and transferred to a clean ultracentrifuge tube. The collected synaptosome fraction was diluted with 9mL of homogenization buffer and spun at 20,000g for 30 mins at 4°C with the resultant pellet being comprised of isolated synaptosomes (SPM). To release synaptic vesicles from the synaptosomes, the SPM was resuspended in HB and osmotically lysed using 9 volumes of ice-cold water and 3 strokes with a Dounce homogenizer. The solution (S2 or SPM) was layered onto a second sucrose stepwise sucrose gradient (0.4 M/0.6 M/0.8 M/1.0 M/1.2M). Samples were spun at 54,000g for 90 mins at 4°C. SVs were in the fraction above the 0.4M sucrose layer. This layer was collected via syringe with an 18G needle and transferred to a clean ultracentrifuge tube, and spun at 200,000g for 2 h at 4°C. Pellets were resuspended in insoluble lysis buffer (8% SDS+8M Urea) and separated by SDS-page for downstream analysis by western blot. Fractions were identified with the following markers: anti-CoxIV (ab14744, Abcam) mitochondria, anti-Rab7(9367, Cell Signaling) late endosomes, anti-EEA1 (ab109110, AbCam) early endosome, anti-PSD95 (124011, Synaptic Systems) synaptosomes, anti-SYP (101006, Synaptic Systems) synaptic vesicles, as well as anti-Cyclin B1 (ab32053, AbCam for human sample or 4138, Cell Signaling for mouse and rat samples), and anti-MSI2 (ab76148, AbCam) for cytosolic control markers.

Metabolomic analysis

Cells were labeled with either U-C^{13}-Glucose for 24 h or [1,2]-C^{13}-Glucose for 3 h prior to lysis and extraction in methanol:water (80:20, v/v). Metabolite analysis by Reversed-Phase Ion-Pair (RPIP) Mass Spectrometry was performed in negative mode by the Calgary Metabolomics Research Facility (CMRF), supported by the International Microbiome Center and the Canada Foundation for Innovation according to established protocols.[84] Briefly, metabolic analysis is performed on a Q Exactive Hybrid Quadrupole-Orbitrap Mass Spectrometer (Thermo-Fisher) coupled to a Vanquish UHPLC System (Thermo-Fisher). Chromatographical separation of metabolites is performed on Zorbax SB-C18 UHPLC column (2.1 mm × 50 mm x 1.8um, Agilent, Part number 822700-902) at the flow rate of 600uL/min using a binary solvent system: solvent A, 10mM tributylamine, 10mM acetate pH 7.5 in 97/3% (v/v) mass spectrometry grade water/methanol and solvent B, mass spectrometry grade acetonitrile. The gradient is 0 min, 0% B; 1 min, 0% B; 2 min, 25% B; 3.5 min, 25% B; 5 min, 55% B; 6.5 min, 55% B; 8.5 min, 100% B; 10 min, 100% B; 11 min, 0% B. Sample injection volume is 2uL. The mass spectrometer is run in negative full scan mode at a resolution of 140,000 scanning from 50 to 750m/z. Metabolite data is analyzed by El-MAVEN software package.[85,86] Metabolites is identified by matching observed m/z signals (+/−10ppm) and chromatographic retention times to those observed from commercial metabolite standards (LMSLS Sigma-Aldrich).

Western Blot analysis

Briefly, samples were separated on 4–12% gradient Bis-Tris SDS-PAGE gel and either stained with Coomassie brilliant blue or transferred onto 0.2 μm nitrocellulose. Membranes were probed with the following primary antibodies that were used at a dilution of 1:1000 unless otherwise indicated: anti-β-actin (A5441, Sigma), anti-α-syn (610787, BD Biosciences), anti-*α-syn*-PS129 (1:10000, ab51253, Abcam), anti-G6PD (66373-1, ProteinTech (for human sample) or PA5-29662 (for mouse and rat samples) Invitrogen), anti-PGLS (PA5-59732 (for human sample) or PA5-98053 (for mouse and rat samples), Invitrogen), and anti-PGD (ab129199, Abcam). When Donkey anti-mouse (BioRad, Mississauga, ON, Canada, 1:2000) and anti-rabbit (BioRad, Mississauga, ON, Canada, 1:2000) HRP conjugated secondary antibodies were used, Clarity or Clarity Max western ECL blotting substrate (Bio-Rad, Mississauga, ON,

Canada) was used to visualize bands on blots. When anti-mouse (800) and anti-rabbit (700) Li-Cor infrared conjugated secondary antibodies were used (1:5000), bands were visualized on the Li-Cor Fc imaging platform. Densitometry was performed to quantify band intensity using the Li-Cor Fc program.

Dopamine analysis

DA levels were measured by HPLC as previously described.[87] In brief, one 10cm plate per condition of differentiated human DA neurons was homogenized in 200μL of 0.2M perchloric acid containing 3 mM cysteine. After 20 dounce strokes, the homogenate was centrifuged (12,000 × g, 10 min,4°C), and the resulting supernatant was left on ice for 5 min, prior to HPLC with fluorescent detection. 1 μL hN-derived extract or 1 μL of purified DA standard (0.1–100 μg/mL) was injected in a Spherisorb ODS2 Waters C18 chromatography column (250 × 4.6mm: 5μm) with in acetate buffer (12 mM Acetic acid, 0.26 mM Na_2EDTA):Methanol (86:14 v/v) as mobile phase at 1 mL/min. The fluorescence was monitored at excitation and emission wavelengths of λ 279 nm and λ 320 nm, respectively. Dopamine was eluted at 11.9 min. The linear range of detection was between 0.00625 μg/mL and 0.25 μg/mL. Data were fitted to a linear formula (y = 4.0974x) for absolute quantification of nmoles of dopamine and normalized to total protein content.

nIRF analysis of Ox-DA protein adducts

This method utilizes the specific inherent excitation–emission properties of o-quinones in the near-infrared spectrum and allows for rapid and absolute quantification into the picomole range as described.[88,89] Briefly, one 10cm plate of hN DA neurons per condition were scrapped in cold PBS and centrifuged at 400g for 5 min. The cell pellet was homogenized in 1mL lysis buffer (% Triton X-100, 10% glycerol, 150mM NaCl, 25mM HEPES pH7.4, 1mM EDTA, 1.5mM $MgCl_2$ and proteinase/phosphatase inhibitors) via sonication 3 pulses, 1sec, 20% amplitude (Q700, Thermo). Samples were spun at 100,000x g (51,000rpm TLA-100) for 30min. 900ul 2% SDS buffer (2% SDS 50mM Tris pH 7.4) was added to insoluble pellets, which were then boiled for 10mins and sonicated 3 pulses, 1 s, 20% amplitude to reconstitute. Samples were spun at 150,000x g (60,000rpm TLA-100) for 30min; pellets were resuspended in 100μL of 1M NaOH and incubated at 55°C overnight. Samples were then frozen in LN2 for 15 min and lyophilized until the pellet was completely dry (1–2 h). The pellet was then washed once with 200ul Nanopure H2O for removal of hydroxides and to lower pH levels and lyophilized again before being resuspended in 50ul Nanopure H2O. 10 μL of sample or DOPAC-*o*-quinone standard, 0.5–50 nmol, (Sigma, #D9628) was loaded onto a Biodyne Nylon Transfer Membrane (Pall, #Pall-60209) and scanned using an Odyssey infrared imaging system (LI-COR) with the 700 channel. Samples were quantified by obtaining integrated spot intensities using Odyssey infrared imaging software, v.3.1. Data were fitted to the polynomial formula $y = 0.084X^2+4.37X+1.4$ for absolute quantification of nmol oxidized dopamine.

G6PD activity, GSH and NADPH analysis

G6PD activity was measured using a fluorometric enzyme activity assay (ab176722, Abcam) in accordance with the manufacturer's protocol. Either recombinant G6PD (10096-DH, R&D Systems) in the presence and absence of recombinant monomeric α-syn or α-*syn*-PFFs was incubated with the provided reaction mix (enzyme substrate solution) and incubated for 30 min and fluorescence was measured using (Ex/Em = 540/590 nm) using a FLUOstar Omega plate reader with Omega V5.70 software in kinetic mode. Alternatively, neurons were washed in ice-cold PBS, homogenized by passing through an 18G needle, and pelleted at 14000g for 5 min at 4°C. Supernatant was then analyzed as described above relative to known enzyme standards. For the determination of free GSH as well as GSH/GSSG ratios, a colorimetric detection method was employed (Glutathione Colorimetric Detection Kit, EIAGSHC Invitrogen). Briefly, samples were washed in ice-cold PBS prior to being lysed and deproteinized with 5% Sulfosalicylic acid to prevent further GSH oxidation. Samples were lysed by sonication, 3 pulses, 1sec, 20% amplitude (Q700, Thermo) and then spun at 9000g for 10 min at 4C. The supernatant was processed as per the manufacturer's protocol and diluted 1:20 with 1X Assay Buffer. Colorimetric readouts for Total GSH (non-VP2 treated) and GSSG (VP2 treated) were individually measured at 405nm following a 20 min incubation period along with GSH and GSSH standards. Free glutathione (Free GSH) concentrations are determined by subtracting the GSSG concentration from values obtained from the total GSH. For $NADPH^+/H^+$ analysis was performed Using Abcam Fluorometric NADP/NADPH Assay Kit (ab176724) according to the manufacturer's protocol. Briefly, human DA neurons or mouse striatal tissue was washed with ice-cold PBS and homogenized with supplied lysis buffer. Samples were spun at 2500 rpm for 10 min at room temperature. The supernatant was directly assayed for NADPH and NADP through the addition of appropriate extraction buffers (provided) and following a 60-min incubation, fluorescence increase was measured at Ex/Em = 540/590 nm using a FLUOstar Omega plate reader with Omega V5.70 software. Data were normalized to total protein content of each sample.

Alpha fold predictions

Deep learning prediction and structural modeling of the interaction between G6PD and α-syn were initially generated with AlphaFold3 using the 'ColabFold' Google Colab page.[90,91] 20 models of each interaction were generated and a single model was selected based on ptm (protein folding score) and iptm (protein folding/interaction score) scores as well as structural similarity to their unbound protein counterparts. Models were visualized, and electron clouds were generated with the molecular display features of ChimeraX v1.6.1.

Slot blot ELISA

Validation of the G6PD/α-syn interaction and binding kinetics were established by loading 200μL of 2μM recombinant G6PD into the slot blot apparatus (Bio-Rad). The sample was allowed to enter the apparatus by gravity for 10 min before vacuum was applied.

Following sample loading, wells were washed using 400 μL PBS. Subsequently, the membrane was removed from the slot blot apparatus and blocked using 5% milk in PBS for 1 h. To test the binding of α-syn, membranes were incubated with increasing molar ratios (1:1, 10:1 or 100:1) monomeric WT-α-syn, ΔCTerm-α-syn or α-*syn*-PFF for 1 h at 37°C with shaking. The membrane was then washed 3x with PBS with 0.1% tween and incubated with primary antibody α-syn (610787, BD Biosciences, 1:1000) or G6PD (PA5-25017, Invitrogen, 1:1000). Licor infrared conjugated secondary antibodies (donkey-*anti*-rabbit or donkey-*anti*-mouse, 1:2000) were used and densitometry was performed to quantify band intensity using Li-Cor Fc. Intensities were fitted by a non-linear regression model.

Isothermal titration calorimetry (ITC)

The characterization of G6PD– α-syn interaction was performed by titration of WT-α-syn into glucose-6-phosphate dehydrogenase (G6PD) using an Affinity ITC Low Volume (TA instruments) machine. Both proteins were in PBS buffer and 100 μM NADP, at a pH of 7.4. The upper isotherm represents the ITC measurements conducted at 37°C in which thirty 2 μL titrations of wild-type α-synuclein (0.5 mM) were injected into G6PD (50 μM) in the cell. The data for each run was processed using NanoAnalyze (Version 3.0, TA Instruments). The lower curve depicts the molar heat values derived from the integration of individual heats as a function of the total molar ratio of protein/protein in the calorimetric cell. The integrated heats from each injection were fit to a two-site binding model to determine the average kinetic parameters of the interaction between α-syn and G6PD.

Floatation assays

Small Unilamellar Vesicles (SUV) were prepared using porcine brain phosphatidylcholine (PC), and porcine brain phosphatidylserine (PS), purchased from Avanti Polar Lipids (Alabaster, AL) and stored at −20°C until use. Aliquots of chloroform solutions of PC and PS were combined at a molar ratio of 60:40 PC:PS. Unilamellar vesicles with a 50-80-nm diameter, referred to as SUVs, were formed as previously described.[92] G6PD flotation experiments were based on a protocol described by Anton and colleagues.[93] Each experiment contained 10 μM of protein (G6PD alone, WT α-syn alone, or G6PD and WT-α-syn) and SUVs in a range of 0 to 1mM (0 mM,0.1 mM, 0.25 mM,0.5 mM, 0.75 mM and 1 mM) in 125 μL potassium phosphate buffer (KPB). Mixtures were incubated at 37°C for 1hr, after which they were mixed with 175 μL of 2.4M sucrose. Using a syringe, 400 μL of 0.8M sucrose and 300 μL of 0.5M sucrose were carefully layered for each tube. Samples were centrifuged at 90,000 rpm for 3 h at 4°C using a TLA-100.3 rotor (Beckmann). Following centrifugations, fractions were collected using a syringe, starting with the bottom 250 μL, containing free protein. The remaining 750 μL was collected as apparently bound protein. Free protein was quantified by Western blot for G6PD and α-syn as described above. Donkey anti-rabbit-800 and donkey anti-mouse-700 Licor secondary antibodies were used at 1:10,000 dilution. Membranes were imaged on a Licor-Fc and quantified using Image studio suite version 5.2 (Licor). Quantitative densitometry was normalized to free protein standards.

Gel mobility shift assays

G6PD and either monomeric WT-α-syn or PFF-α-syn were incubated with 0.04% glutaraldehyde at room temperature for 10 min, at which point they were mixed with 10 μL of Tris-HCl pH 8 and 27.5 μL of 5X Reducing Sample Buffer before being separated on 10% Bis-Tris SDS-PAGE gels and transferred onto 0.2 μm PVDF membranes. Membranes were then probed with total α-syn anti-mouse monoclonal and G6PD anti-rabbit polyclonal primary antibodies. Donkey anti-rabbit-800 Li-Cor secondary antibodies and donkey anti-mouse-700 Li-Cor infrared conjugated secondary antibodies were then used at 1:5000 dilutions. Bands were visualized on blots using the Li-Cor Fc imaging platform and Clarity Western ECL Blotting Substrate [Bio-Rad] in succession. Densitometry was then performed gels to quantify the upward shift in G6PD migration.

UK biobank data analysis

Analysis of UK Biobank datasets was performed using GeneBass (www.genebass.com), which is a browser of summary statistics from a systematic large-scale rare variant association analysis of 4,529 phenotypes with single-variant and gene tests of 394,841individuals in the UKBiobank with exome-sequence data.[34] We searched for associations between G6PD exosome sequencing and Parkinson's Disease phenotype. Significant associations of gene burden of disease, identified missense mutations, and allele frequency were directly extrapolated. We then searched for clinical reports of pathogenicity of each identified missense mutation using the ClinVar database (https://www.ncbi.nlm.nih.gov/clinvar/).[35,36]

QUANTIFICATION AND STATISTICAL ANALYSIS

Data represent at least 3 independent differentiations with at least two replicates, presented as mean +s.e.m. or ± min to max. Statistical significance was ascertained by Principal component analysis, Student t-test or two-way ANOVA with appropriate *post hoc* testing (Dunnett's or Tukey's test); $p < 0.05$ was considered significant. All data were analyzed using Prism7 (Graphpad Software Inc.). For data not fitting a normal distribution, non-parametric tests were used. All of the statistical details of experiments can be found in the figure legends.